High spectral resolution imaging of the dynamical atmosphere of the red supergiant Antares in the CO first overtone lines with VLTI/AMBER

K. Ohnaka, K. -H. Hofmann, D. Schertl, G. Weigelt, C. Baffa, A. Chelli, R. Petrov, S. Robbe-Dubois

A&A 555, A24 (2013)
DOI: 10.1051/0004-6361/201321063

Astronomy & Astrophysics

High spectral resolution imaging of the dynamical atmosphere of the red supergiant Antares in the CO first overtone lines with VLTI/AMBER⋆,⋆⋆,⋆⋆⋆

K. Ohnaka[1], K.-H. Hofmann[1], D. Schertl[1], G. Weigelt[1], C. Baffa[2], A. Chelli[3], R. Petrov[4], and S. Robbe-Dubois[4]

[1] Max-Planck-Institut für Radioastronomie, Auf dem Hügel 69, 53121 Bonn, Germany
e-mail: kohnaka@mpifr.de
[2] INAF – Osservatorio Astrofisico di Arcetri, Instituto Nazionale di Astrofisica, Largo E. Fermi 5, 50125 Firenze, Italy
[3] UJF – Grenoble 1 / CNRS-INSU, Institut de Planétologie et d'Astrophysique de Grenoble (IPAG) UMR 5274, 38041 Grenoble, France
[4] Observatoire de la Côte d'Azur, Departement FIZEAU, Boulevard de l'Observatoire, BP 4229, 06304 Nice Cedex 4, France

Received 8 January 2013 / Accepted 4 April 2013

ABSTRACT

Aims. We present aperture-synthesis imaging of the red supergiant Antares (α Sco) in the CO first overtone lines. Our goal is to probe the structure and dynamics of the outer atmosphere.
Methods. Antares was observed between 2.28 μm and 2.31 μm with VLTI/AMBER with spectral resolutions of up to 12 000 and angular resolutions as high as 7.2 mas at two epochs with a time interval of one year.
Results. The reconstructed images in individual CO lines reveal that the star appears differently in the blue wing, line center, and red wing. In 2009, the images in the line center and red wing show an asymmetrically extended component, while the image in the blue wing shows little trace of it. In 2010, however, the extended component appears in the line center and blue wing, and the image in the red wing shows only a weak signature of the extended component. Our modeling of these AMBER data suggests that there is an outer atmosphere (MOLsphere) extending to 1.2–1.4 $R_\star$ with CO column densities of (0.5–1) $\times$ 10^{20} cm^{-2} and a temperature of ~2000 K. The CO line images observed in 2009 can be explained by a model in which a large patch or clump of CO gas is infalling at only 0–5 km s^{-1}, while the CO gas in the remaining region is moving outward much faster at 20–30 km s^{-1}. The images observed in 2010 suggest that a large clump of CO gas is moving outward at 0–5 km s^{-1}, while the CO gas in the remaining region is infalling much faster at 20–30 km s^{-1}. In contrast to the images in the CO lines, the AMBER data in the *continuum* show only a slight deviation from limb-darkened disks and only marginal time variations. We derive a limb-darkened disk diameter of 37.38 ± 0.06 mas and a power-law-type limb-darkening parameter of (8.7 ± 1.6) $\times$ 10^{-2} (2009) and 37.31 ± 0.09 mas and (1.5 ± 0.2) $\times$ 10^{-1} (2010). We also obtain an effective temperature of 3660 ± 120 K (the error includes the effects of the temporal flux variation that is assumed to be the same as Betelgeuse) and a luminosity of $\log L_\star/L_\odot$ = 4.88 ± 0.23. Comparison with theoretical evolutionary tracks suggests a mass of 15 ± 5 $M_\odot$ with an age of 11–15 Myr, which is consistent with the recently estimated age for the Upper Scorpius OB association.
Conclusions. The properties of the outer atmosphere of Antares are similar to those of another well-studied red supergiant, Betelgeuse. The density of the extended outer atmosphere of Antares and Betelgeuse is higher than predicted by the current 3D convection simulations by at least six orders of magnitude, implying that convection alone cannot explain the formation of the extended outer atmosphere.

Key words. infrared: stars – techniques: interferometric – stars: late-type – stars: atmospheres – stars: individual: Antares – supergiants

1. Introduction

The mass loss in the red supergiant (RSG) stage significantly affects the final fate of massive stars. For example, the mass loss in the RSG stage seems to be a key to understanding the progenitors of the most common core-collapse supernovae (SNe) Type IIp (e.g., Smartt et al. 2009). However, the mass loss in RSGs is still poorly understood. As Harper (2010) stresses, there are currently no satisfactory theories for the RSG mass loss. Even the driving force of the stellar winds has not yet been identified.

For understanding the wind acceleration mechanism, it is important to study the region between the photosphere and the innermost circumstellar envelope, where the stellar winds are expected to be accelerated. Various observations suggest the complicated nature of this region. Tuthill et al. (1997) have discovered asymmetric structures on the surface of three well-studied RSGs, Betelgeuse (α Ori), Antares (α Sco), and α Her. They interpret these asymmetric structures as the presence of one to three hot spots. The recent near-IR interferometric observations of Betelgeuse by Haubois et al. (2009) also show surface inhomogeneities. The detection of H_2O in Betelgeuse and Antares at 12 μm (Jennings & Sada 1998), as well as in the near-IR and in the 6 μm region (Tsuji 2000a,b), suggests

⋆ Based on AMBER observations made with the Very Large Telescope Interferometer of the European Southern Observatory. Program ID: 083.D-0333(A/B) (AMBER guaranteed time observation), 085.D-0085(A/B).
⋆⋆ Appendices are available in electronic form at http://www.aanda.org
⋆⋆⋆ Movies of data cube are only available at the CDS via anonymous ftp to cdsarc.u-strasbg.fr (130.79.128.5) or via http://cdsarc.u-strasbg.fr/viz-bin/qcat?J/A+A/555/A24

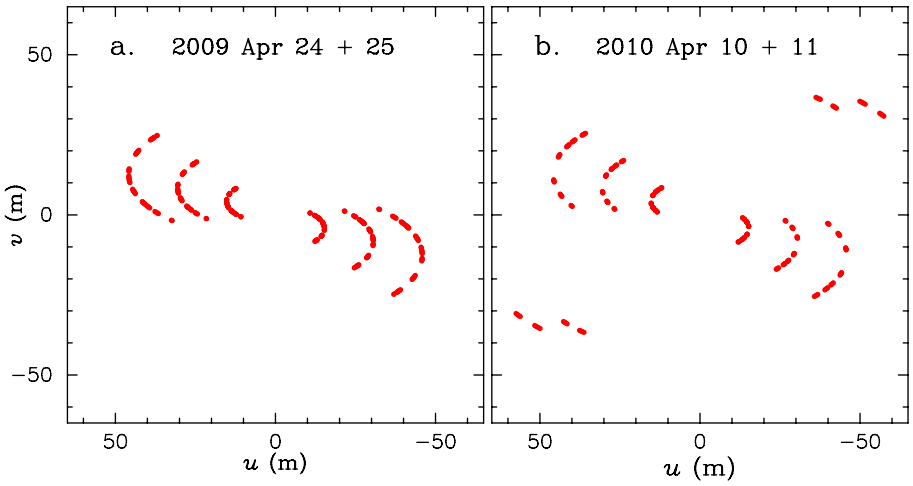

Fig. 1. *uv* coverage of our AMBER observations of Antares in 2009 **a)** and 2010 **b)**.

that there is an outer atmosphere extending to 1.3–2 stellar radii with temperatures of 1500–2000 K, the so-called MOLsphere as coined by Tsuji (2000b).

The radio observations of Betelgeuse and Antares also show neutral gas extending to several stellar radii (Lim et al. 1998; Harper et al. 2010). On the other hand, spatially resolved observations of RSGs in the UV, as well as in the Hα line, suggest that the chromosphere also extends to several stellar radii (Gilliland & Dupree 1996; White et al. 1982; Hebden et al. 1987). Harper et al. (2001) propose that the chromosphere has a small filling factor embedded in the neutral/molecular gas. However, the physical mechanism responsible for this inhomogeneous, multicomponent outer atmosphere is by no means clear. Inhomogeneous structures are also found farther out from the star. The near- and mid-IR imaging of Betelgeuse (Kervella et al. 2009, 2011) and Antares (Bloemhof et al. 1984; 1995; Marsh et al. 2001) reveals a clumpy structure of the circumstellar envelope.

For a better understanding of the mass-loss mechanism in RSGs, it is essential to probe the dynamics of the inhomogeneous, multicomponent outer atmosphere. We carried out high spatial and high spectral resolution observations of Betelgeuse in the CO first overtone lines near 2.3 μm using VLTI/AMBER (Ohnaka et al. 2009; 2011, hereafter Papers I and II, respectively). With the stellar disk spatially resolved with an angular resolution of 9.8 mas (the highest resolution ever achieved at any wavelength for this well-studied star), AMBER's high spectral resolution of up to 12 000 enabled us to spatially resolve, for the first time, the gas motions over the surface of a star other than the Sun. These AMBER observations have revealed that the star appears differently in the blue and red wings of the individual CO lines due to an inhomogeneous velocity field in the photosphere and MOLsphere.

In this paper, we present high spectral and high spatial resolution VLTI/AMBER observations of another well-studied RSG, Antares (M1.5Iab-b), in the CO first overtone lines. Antares is similar to Betelgeuse (M2Iab:) in terms of the spectral type, although it is slightly less luminous and less massive than Betelgeuse (see Sect. 3.2). The mass-loss rate of Antares is estimated to be $\sim 2 \times 10^{-6}$ $M_\odot$ yr^{-1} (Braun et al. 2012), which is comparable to that of Betelgeuse ($\sim 3 \times 10^{-6}$ $M_\odot$ yr^{-1}, Harper et al. 2001). However, the IR excess and the 10 μm silicate emission of Antares are much weaker than those of Betelgeuse (e.g., Monnier et al. 1998; Verhoelst et al. 2009). Our goal is to spatially resolve the gas motions in the outer atmosphere in this second RSG and to examine whether the findings for Betelgeuse are common among RSGs. The paper is organized as follows. The observations and data reduction as well as image reconstruction from the interferometric data are described in Sect. 2. We present the results in Sect. 3 followed by the modeling of the data in Sect. 4 and the interpretation of the results in Sect. 5. Conclusions are given in Sect. 6.

2. Observations

2.1. AMBER observations and data reduction

AMBER (Petrov et al. 2007) is a VLT spectro-interferometric instrument that operates in the near-IR (1.3–2.4 μm) and combines three 8.2 m Unit Telescopes (UTs) or 1.8 m Auxiliary Telescopes (ATs). AMBER records spectrally-dispersed interferograms with a spectral resolution of up to 12 000. AMBER measures the amplitude of the Fourier transform (so-called visibility or visibility amplitude), closure phase (CP) and differential phase (DP), with the usual (i.e., spatially unresolved) spectrum. The CP is the sum of the measured Fourier phases around a closed triangle of baselines (i.e., $\varphi_{12} + \varphi_{23} + \varphi_{31}$), which is not affected by the atmospheric turbulence. Therefore, it is essential for aperture-synthesis imaging in optical/IR interferometry. The CP is zero or π for point-symmetric objects and non-zero and non-π CPs indicate an asymmetry of the object. The DP provides information about the wavelength dependence of the photocenter shift of the object within spectral features.

Antares was observed on 2009 April 24 and 25 and, one year later, on 2010 April 10 and 11, with AMBER using the E0-G0-H0 (16–32–48 m) array configuration and the E0-G0-I1 (16–57–69 m) configuration (Program IDs: 083.D-0333, 085.D-085, P.I.: K. Ohnaka). As in Papers I and II, we used the high resolution mode in the K-band (HR_K) with a spectral resolution of 12 000 and covered wavelengths from 2.28 to 2.31 μm to observe the CO first overtone lines near the (2, 0) band head. We detected fringes on all three baselines without using the VLTI fringe tracker FINITO (Antares saturates FINITO) thanks to the extremely high brightness of Antares ($K = -4.1$). In 2009 and 2010, we observed on two half nights each and obtained 65 and 44 data sets, respectively. The data sets taken more than ~2 min apart were treated as separate data sets, because Antares is strongly resolved, and the visibility varies noticeably even with a slight change in the projected baseline length (see Fig. 3). Figure 1 shows the *uv* coverage of our observations in 2009 and 2010. All data sets were taken with a detector

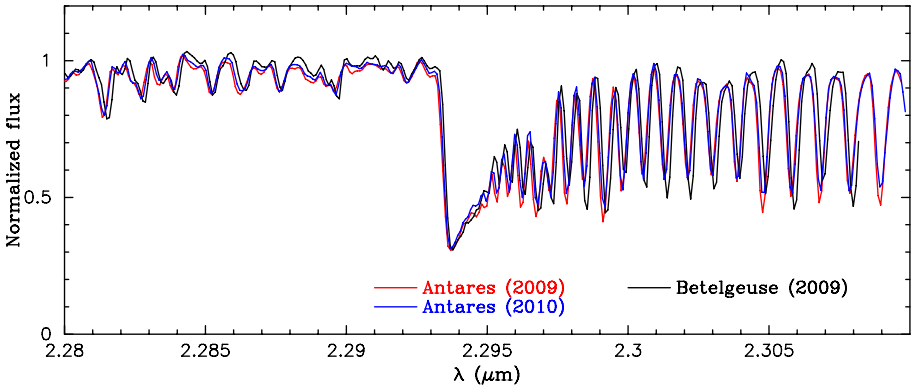

Fig. 2. Spectra of Antares observed in 2009 and 2010, together with the spectrum of Betelgeuse from Paper II (the one obtained in 2009).

integration time (DIT) of 130 ms. A summary of the observations is given in Tables A.1 and A.2.

For the reduction of the AMBER data, we used amdlib ver. 2.2[1], which is based on the P2VM algorithm (Tatulli et al. 2007). In order to improve the signal-to-noise ratios (S/N), we applied a binning in the spectral direction to all the raw data (object, dark, sky, and P2VM calibration data) using a running box car function as described in Paper I. The binning down to a spectral resolution of 8000 provided an S/N sufficient for the image reconstruction. One of the parameters in the reduction with amdlib is the frame selection criterion. In each data set, we checked for a systematic difference in the calibrated results by taking the best 20%, 50%, and 80% of all frames in terms of the fringe S/N (Tatulli et al. 2007). The difference between the results obtained with the best 20% and 80% of frames is negligible, and therefore, we took the best 80% of all frames for our final results. The errors of the resulting visibilities, DPs, and CPs were estimated in the manner described in Paper I.

α Cen A (G2V) and α Cen B (K1V) were observed for the calibration of the interferometric data of Antares. α Cen is a triple system consisting of α Cen A, α Cen B, and Proxima Cen. However, we always had only one component (A or B) in the field of view of AMBER. We adopted angular diameters of 8.314 ± 0.016 and 5.856 ± 0.027 mas derived by Kervella et al. (2003) for α Cen A and B, respectively. We also used α Cen A as a spectroscopic standard star to remove telluric lines from the observed spectra of Antares. However, the spectrum of α Cen A shows weak CO first overtone lines. In this case, as described in Ohnaka et al. (2012), the calibrated spectrum of the science target is derived as $F_\star^{\rm sci} = F_{\rm obs}^{\rm sci}/(F_{\rm obs}^{\rm cal}/F_\star^{\rm cal})$, where $F_\star^{\rm sci(cal)}$ and $F_{\rm obs}^{\rm sci(cal)}$ denote the true and observed (i.e., including the atmospheric transmission and the detector's response) spectra of the science target (or calibrator), respectively. We used the high resolution solar spectrum presented by Wallace & Hinkle (1996) to estimate the true spectrum of the calibrator α Cen A, because this star has the same spectral type as the Sun.

The wavelength calibration was done by using the telluric lines in the spectrum of α Cen A. As a template of the telluric lines, we convolved the atmospheric transmission spectra measured at the Kitt Peak National Observatory[2] to match the spectral resolutions of the data. The uncertainty in wavelength calibration is 1.7×10^{-5} μm (~2 km s^{-1}). The wavelength scale was converted to the heliocentric frame and then to the laboratory frame using the heliocentric velocity of -3.5 km s^{-1} measured for Antares (Gontscharov 2006). Figure 2 shows the spectra of Antares observed in 2009 and 2010, together with the spectrum of Betelgeuse obtained in 2009 (Paper II). These spectra are binned to the same spectral resolution of 8000. The observed spectra of Antares are similar to that of Betelgeuse and show little time variation within an interval of one year. However, despite this absence of time variation in the observed spectra, our spectro-interferometric observations have detected significant time variation in the velocity field of the atmosphere, as presented in Sect. 3.3.

2.2. Image reconstruction

We used the MiRA package ver.0.9.9[3] (Thiébaut 2008) to reconstruct an image from the interferometric measurements at each spectral channel. As described in Paper II, we first carried out the image reconstruction using simulated data. As described in Appendix B, we generated simulated stellar images (e.g., limb-darkened disk or stellar disk with inhomogeneities and/or an extended component) and computed visibilities and CPs with realistic noise at the same *uv* points as in our AMBER observations of Antares. With the true image known, we searched for the appropriate reconstruction parameters, such as the initial model and regularization scheme. We also applied the self-calibration technique described in Paper II, which restores the Fourier phase from the differential phase measurements.

3. Results

3.1. Continuum data

We selected the continuum spectral channels shortward of the CO band head at 2.295 μm, avoiding the CO lines as well as the weak lines. The average visibilities over the continuum spectral channels were computed in each data set. We adopted the simple mean of the errors without reducing by $\sqrt{N_{\rm cont}}$, where $N_{\rm cont}$ is the number of the continuum spectral channels, because the errors are dominated by systematic errors, and they do not become smaller by averaging.

Figure 3 shows the continuum visibilities measured in 2009 and 2010. The 2009 and 2010 data sample up to the fourth and fifth visibility lobes, respectively. This corresponds to angular resolutions of 9.8 and 7.2 mas for the 2009 and 2010 data, respectively, which mark the highest spatial resolution achieved for Antares at any wavelength. Uniform-disk fits to the 2009 and 2010 data result in 36.97 ± 0.05 mas (reduced $\chi^2 = 4.6$) and

[1] Available at http://www.jmmc.fr/data_processing_amber.htm

[2] http://www.eso.org/sci/facilities/paranal/instruments/isaac/tools/spectra/atmos_S_K.fits

[3] http://www-obs.univ-lyon1.fr/labo/perso/eric.thiebaut/mira.html

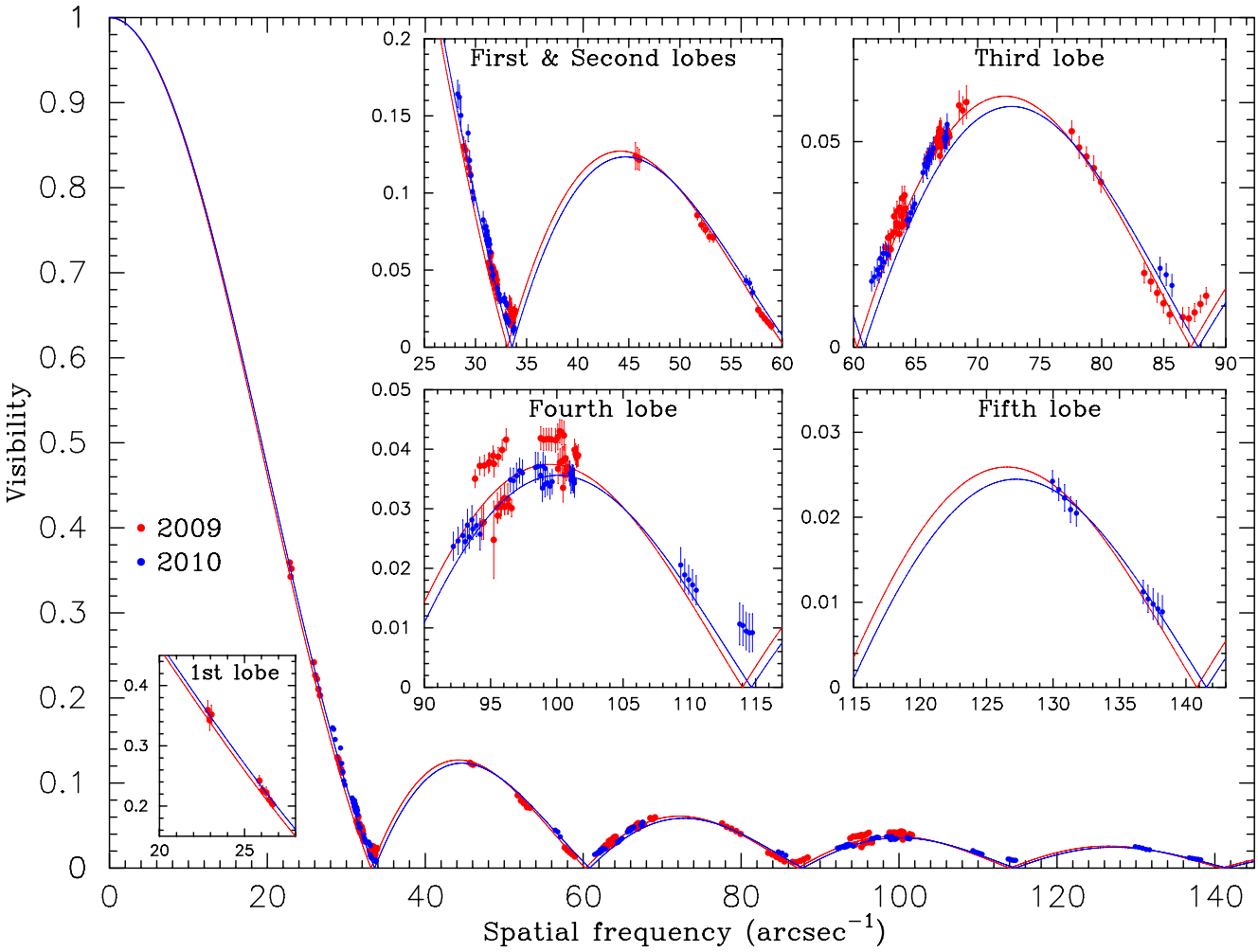

Fig. 3. *K*-band continuum visibilities of Antares observed in 2009 (red dots) and 2010 (blue dots). The fit with the power-law-type limb-darkened disk for the 2009 and 2010 data is shown by the red and blue solid lines, respectively. The limb-darkened disk has angular diameters of 37.38 and 37.31 mas and limb-darkening parameters of 0.087 and 0.15 for the 2009 and 2010 data, respectively. The insets show the enlarged views of the individual visibility lobes.

36.50 ± 0.05 mas (reduced χ^2 = 5.4), respectively. Fitting with a power-law-type limb-darkened disk (Hestroffer et al. 1997) results in a limb-darkened disk diameter of 37.38 ± 0.06 mas and a limb-darkening parameter of $(8.7 \pm 1.6) \times 10^{-2}$ for the 2009 data and 37.31 ± 0.09 mas and $(1.5 \pm 0.2) \times 10^{-1}$ for the 2010 data (the errors were estimated by the bootstrapping technique as described in Efron & Tibshirani 1993).

The reduced χ^2 values for the fit to the 2009 and 2010 data are 3.9 and 3.3, respectively. These values are better than those with the uniform-disk fit but are still higher than 1. This is because of the deviation from the limb-darkened disks in the data points at visibility nulls at spatial frequencies of ∼87 arcsec^{-1} (2009 data) and ∼115 arcsec^{-1} (2010 data), as well as those at 95–100 arcsec^{-1} in the 2009 data. These last data points were obtained at position angles differing by 20–25°, which suggests the presence of inhomogeneities on a spatial scale of ∼10 mas in 2009. However, as discussed in Sect. 3.3, the reconstructed images in the continuum show only a very slight deviation from the limb-darkened disk: less than 2% (see Fig. 5i). The 2010 data include *uv* points taken at position angles differing by roughly 90°, which are located at spatial frequencies of 130–138 arcsec^{-1}. Still, Fig. 3 shows that the measured visibilities closely follow the limb-darkened disk. In summary, the overall deviation from the limb-darkened disks is small, indicating that the star shows only a weak signature of inhomogeneities in the continuum. Comparison between the 2009 and 2010 data suggests that a time variation with an interval of one year is only marginal. The same finding in Betelgeuse is reported in Paper II. Therefore, RSGs may show only a small deviation and time variation in the surface structure seen in the continuum.

This observed time variation (or absence of it) is much smaller than the maximum visibility variation of ±40% predicted by the current 3D convection simulations in the third lobe for 2.2 μm, which approximately samples the continuum (see Fig. 18 of Chiavassa et al. 2009). However, this does not necessarily mean that the observed time variation disagrees with the 3D simulations. It is possible that we observed Antares at two epochs with small variations by chance, given that the 3D simulations of Chiavassa et al. (2009) show that large convective cells have lifetimes of years. Furthermore, the standard deviation of the temporal variation in the visibility predicted by the 3D simulations is smaller than 40%, down to 10%, depending on the spatial frequency (see Figs. 11, 12, and 14 of Chiavassa et al. 2009). It is also possible that significant inhomogeneities remained undetected due to the limited position angle coverage of our observations. Therefore, long-term monitoring AMBER observations with better position angle coverage are necessary to rigorously test the current 3D convection simulations.

The derived limb-darkened disk angular diameters are noticeably smaller than the 41.3 ± 0.1 mas derived from lunar occultation measurements of Richichi & Lisi (1990). However, they used a narrow-band filter at 2.43 μm with a FWHM of 0.035 μm. A number of CO first overtone lines and possibly also H_2O lines from the MOLsphere are present in this wavelength range, which makes the star appear larger than in the continuum. Furthermore, Richichi & Lisi (1990) detected asymmetry in the brightness profile reconstructed from the lunar occultation data. This also indicates that their angular diameter is affected by the inhomogeneous outer atmosphere, where the CO and H_2O molecules form.

3.2. Determination of basic stellar parameters

By combining the above angular diameters in the continuum with the measured bolometric flux, we can determine the effective temperature. We collected photometric data from the U band to 10 μm from the literature (Lee 1970; Ducati 2002; 2MASS, Skrutskie et al. 2006). The photometric data were dereddened by the interstellar extinction, which was estimated as follows. The intrinsic $B - V$ color of an RSG with the spectral type of Antares (M1.5Iab-b) is 1.70 (Elias et al. 1985). On the other hand, the observed $B - V$ color of Antares is 1.84 (Ducati 2002). Therefore, the color excess $E(B - V)$ due to the interstellar extinction is 0.14, which translates into $A_V = 0.43$ if $A_V = 3.1E(B - V)$ (Savage & Mathis 1979) is assumed. Using this interstellar extinction, we derived a dereddened bolometric flux of 8.36×10^{-8} W m^{-2}. The irregular variability of Antares with an amplitude of ∼1 mag in the visible leads to an uncertainty in the bolometric flux, because the photometric data collected from the literature were not taken simultaneously. However, the time variation in flux between the R and K bands is difficult to estimate from the data available in the literature, because the data points are not sufficient. Therefore, we checked the time variation in flux in these bands for Betelgeuse and adopted it for Antares. We estimated the amplitude of the time variation in the R- and I-band flux of Betelgeuse to be 15% based on the photometric data from Ducati (2002) and Low et al. (1970). The light curves at 1.25, 2.2, 3.5, and 4.9 μm obtained over 3.6 years with COBE/DIRBIE suggest that the amplitude of the flux variation is approximately 10% in these IR bands (Price et al. 2010). With these flux variations adopted for Antares, the uncertainty in the bolometric flux is estimated to be $\pm 1.07 \times 10^{-8}$ W m^{-2}.

The limb-darkened disk diameters derived from our AMBER continuum data and this bolometric flux result in an effective temperature of 3660 ± 120 K for both 2009 and 2010. This effective temperature agrees well with the effective temperature scale of Levesque et al. (2005), which gives 3710 K for the spectral type of Antares (M1.5). By combining the measured bolometric flux and the parallax of 5.89 ± 1.00 mas (van Leeuwen 2007), we derive a luminosity of $\log L_\star/L_\odot = 4.88 \pm 0.23$. The linear radius estimated from the measured limb-darkened disk angular diameters and the parallax is 680 $R_\odot$ (3.2 AU). The effective temperature and luminosity we derived agree very well with $T_{\rm eff} = 3707 \pm 77$ K and $\log L_\star/L_\odot = 4.99 \pm 0.15$ derived by Pecaut et al. (2012).

The observationally derived location of Antares on the H-R diagram is shown in Fig. 4 with the theoretical evolutionary tracks for 9, 12, 15, 20, and 25 $M_\odot$ stars for the solar metallicity $Z = 0.014$ published in Ekström et al. (2012). The location of Antares agrees with the evolutionary tracks for a 15 $M_\odot$ star. However, given the large uncertainty in the luminosity, the error in the initial stellar mass is estimated to be ±5 $M_\odot$. This value

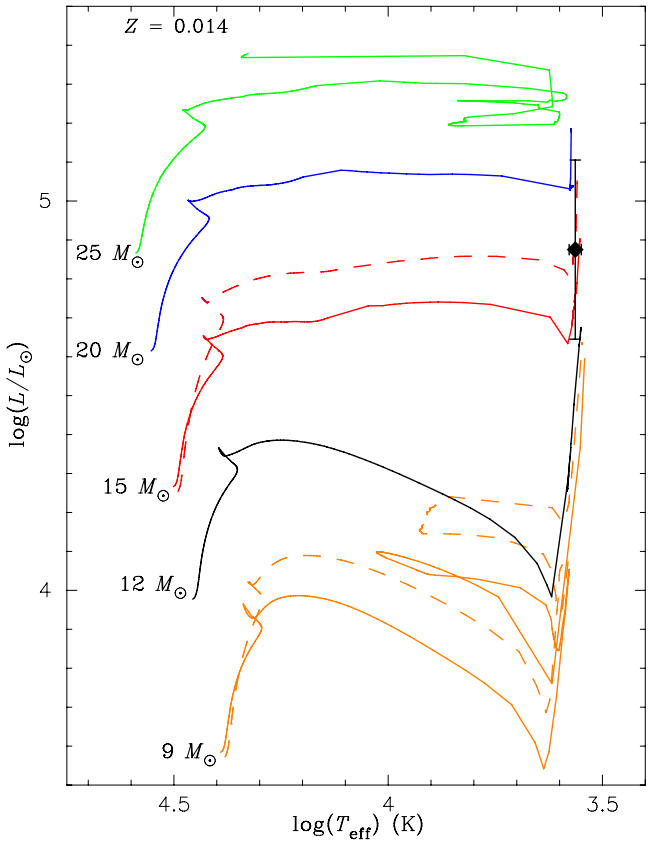

Fig. 4. H-R diagram with the theoretical evolutionary tracks for 9, 12, 15, 20, and 25 $M_\odot$ stars for $Z = 0.014$ without rotation (solid lines) from Ekström et al. (2012) and the observationally derived position of Antares (filled diamond with error bars). For the 15 and 9 $M_\odot$ stars, the evolutionary tracks with rotation are plotted by the dashed lines.

agrees reasonably well with the 17.2 $M_\odot$ derived by Pecaut et al. (2012), who estimated the mass using the evolutionary tracks with rotation of Ekström et al. (2012). The theoretical evolutionary tracks of Ekström et al. (2012) show that when a 15 $M_\odot$ star reaches the observationally derived effective temperature and luminosity of Antares, the current mass is 13–14.3 $M_\odot$ (without rotation) and 11–14.3 $M_\odot$ (with rotation). Combining the mass of 11–14.3 $M_\odot$ and the linear radius of 680 $R_\odot$, we obtain a surface gravity of $\log g = -0.1 ... -0.2$ (g is given in units of cm s^{-2} throughout the paper).

The age of Antares is important for constraining the Upper Scorpius OB association, which is still controversial. Comparison of the position of Antares on the H-R diagram with the evolutionary tracks of Ekström et al. (2012) for a 15 $M_\odot$ star with and without rotation suggests an age of 11–15 Myr. This agrees very well with the 12^{+3}_{-1} Myr derived by Pecaut et al. (2012), which is not surprising given the good agreement for the effective temperature and luminosity between their results and ours. Pecaut et al. (2012) show that this age of Antares is consistent with the age of the Upper Scorpius OB association of 9–13 Myr derived from stars with other spectral types.

3.3. Reconstructed images

Figure 5 shows the reconstructed images from the 2009 data at four different wavelengths (panels a–d) within the CO line

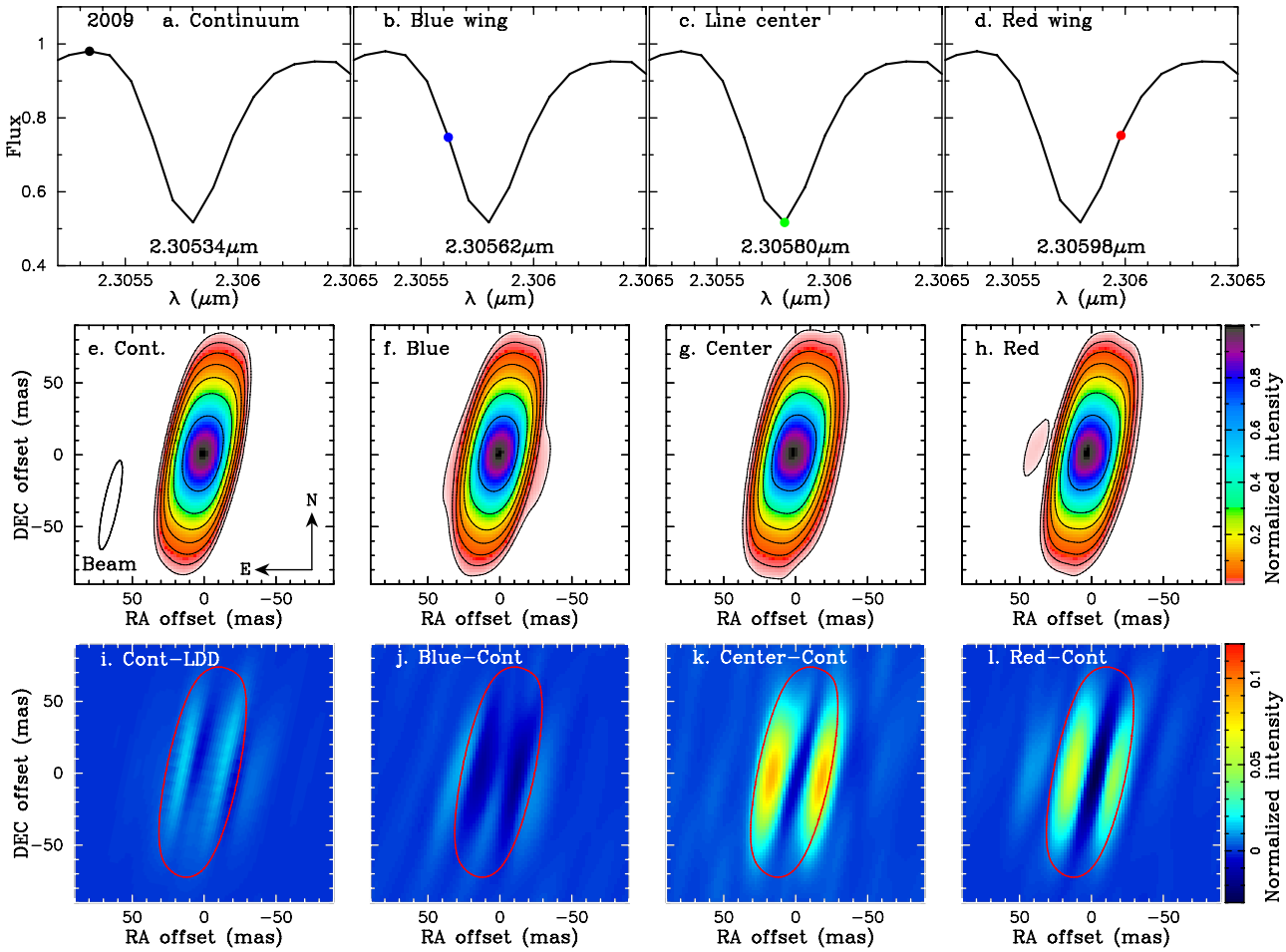

Fig. 5. Reconstructed images of Antares in 2009 within one of the CO first overtone lines (2.3058 μm). Panels **a)**–**d)**: the observed line profile with four representative wavelengths marked. Panels **e)**–**h)** show the images reconstructed at these wavelengths. The contours correspond to 1, 2, 4, 8, 16, 32, and 64% of the peak intensity of each image. Panel **i)** shows the difference between the reconstructed continuum image and the best-fit limb-darkened disk for the continuum visibilities, whose parameters are given in Sect. 3.1. Panels **j)**–**l)** show the continuum-subtracted images, in which the continuum image (panel **e)** is subtracted from the images in the panels **f)**–**h)**. The limb of the star as defined in Sect. 3.3 is marked by the red solid lines.

observed at 2.3058 μm[4]. All reconstructed images appear strongly elongated due to the elongated beam (9.8 × 63.2 mas), which results from the lack of *uv* points roughly in the North-South direction (see Fig. 1). The reconstructed continuum image (Fig. 5e) shows only a slight deviation from the limb-darkened disk that represents the best fit to the continuum visibilities. This is clearly seen in Fig. 5i, which shows the residual continuum image obtained after subtracting the limb-darkened disk with the parameters derived in Sect. 3.1 convolved with the interferometer's beam (the determination of the beam is described in Appendix B). The residuals are at most 2% of the peak intensity of the reconstructed continuum image.

The image in the blue wing (Fig. 5f) appears very similar to that in the continuum except for the very weak extended component on either side of the star. However, the intensity of this extended component is comparable to the noise level of the image reconstruction (∼1%), which is estimated from the intensity of the background features sufficiently away from the star in the reconstructed images. Therefore, it is not clear whether or not this extended component in the blue wing image is real. On the other hand, the images in the line center and red wing (Figs. 5g and 5h) show a much more prominent, asymmetrically extended component.

In order to clearly show the difference among the images, we normalized each image with its peak intensity and subtracted the normalized continuum image from the images within the line. These continuum-subtracted images are shown in the bottom row of Fig. 5. Also plotted is the limb of the star (red solid line), which we define by the contour at 3% of the peak intensity of the continuum image. We adopted this contour because the CO lines appear in emission outside the limb defined in this manner as described below (Fig. 6). Note that we do not artificially adjust the position of the images (either in the lines or in the continuum) at all, because the relative astrometry among the images at different spectral channels is conserved thanks to the self-calibration technique (see Paper II for details). The continuum-subtracted images in the line center and red wing clearly show an extended component that is more prominent on the western side of the star, while the continuum-subtracted image in the blue wing shows almost no extended component. The resolved extended component is present off the limb of the star (i.e., outside the stellar disk) particularly on the western side of the line center image and

[4] A movie of the data cube containing all wavelengths from 2.28 and 2.31 μm is available at http://www.mpifr-bonn.mpg.de/staff/kohnaka

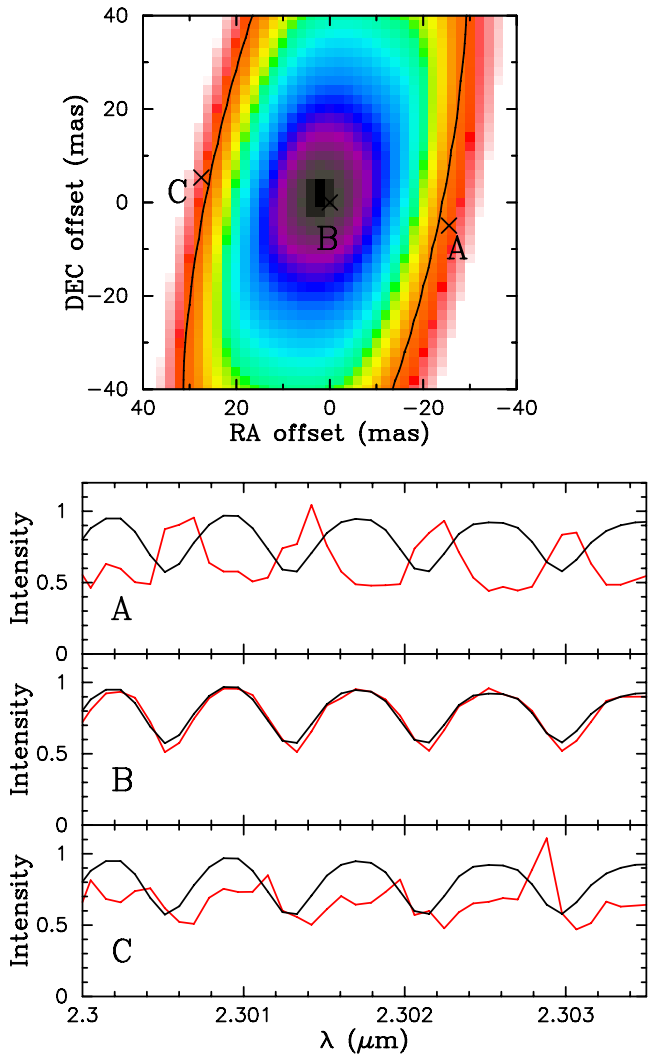

Fig. 6. Spatially resolved spectra obtained in 2009 at three representative positions over the stellar image are plotted by the red solid lines. The representative positions are marked in the top panel, which shows the line center image at 2.30580 μm (same as Fig. 5g). The black lines represent the spatially unresolved spectrum. The spatially resolved spectra are scaled for comparison with the spatially unresolved spectrum. The black solid line in the top panel marks the limb of the star.

also – albeit weaker – in the red wing image. This represents the second imaging of the MOLsphere in RSGs within individual CO lines after Betelgeuse reported in Paper II.

While we normalized each of the above images with its peak intensity, it is also possible to normalize each image so that the intensity integrated over the entire image is equal to the observed flux at that spectral channel. This allows us to extract the spatially resolved spectrum at each position over the stellar image. The spatially resolved 2009 spectra at three representative positions along the direction of the beam's minor axis are shown in Fig. 6, which reveals the CO emission lines off the limb on the western side (position A)[5]. These emission lines are redshifted with respect to the absorption lines in the spatially unresolved observed spectrum, reflecting the appearance of the extended component only in the line center and red wing. On the eastern side, the line profiles are characterized by weak blueshifted emission and redshifted absorption. This is explained as follows. Because of the finite beam size, we see not only the emission off the limb but also the absorption originating from inside the limb. The weak blueshifted emission, which is seen as the weak extended feature in the reconstructed blue wing image (Fig. 5f), partially fills in the absorption. This results in what appears as redshifted absorption with weak blueshifted emission. Ohnaka (2013) presents similar spatially resolved CO first overtone line spectra for Betelgeuse and reveals the CO line emission off the limb, but for the 1D image. Our 2D image reconstruction for Antares demonstrates that it is now feasible to obtain the spatially resolved spectrum at each position over the surface of a star as well as off the limb of the star, as is routinely done in solar physics.

Figure 7 shows the reconstructed images from the 2010 data for the same CO line as shown in Fig. 5. Because the position angle coverage of the 2010 observations is better than the 2009 observations, the beam of the 2010 images is less elongated than that of the 2009 images. However, for a direct comparison of the images taken at two epochs, the 2010 images are convolved with the same beam as used for the images in 2009. The reconstructed image in the continuum shows little deviation from the best-fit limb-darkened disk derived from the continuum visibilities, as in the 2009 data. The residual after subtracting the limb-darkened disk with the parameters derived in Sect. 3.1 is at most 1% of the peak intensity of the reconstructed continuum image. The continuum-subtracted images shown in the bottom row of Fig. 7 reveal that the images in the blue wing and line center show a prominent extended component. On the other hand, the image in the red wing shows little trace of this (the intensity of the extended component in the red wing image is ~2%, which is only slightly higher than the image reconstruction noise of 1%). This means that the appearance of the star in the blue and red wing has swapped within one year (compare the images in the bottom row of Figs. 5 and 7).

Figure 8 shows the spatially resolved spectra at three selected positions over the stellar image. Obviously, the blueshifted emission appears off the limb (position A), although the strength of the emission is weaker than the redshifted emission seen in 2009. This is simply because the extended component, MOLsphere, is weaker in 2010 than in 2009. This can also be seen in the visibilities observed in the first lobe, as shown in Fig. 9. While the observed spatially unresolved spectra show little time variation, the visibilities in the CO lines observed in 2010 are noticeably higher than observed in 2009. This means that the star appears less extended in the CO lines in 2010 than in 2009. The figure also shows the time variation in the visibilities within the CO lines, which corresponds to the different appearance of the star within the CO lines as shown in Figs. 5 and 7.

The time variation in the reconstructed images within the CO lines suggests a significant change in the dynamics of the atmosphere. Such a time variation in the atmospheric dynamics has already been detected in Betelgeuse (Paper II). Therefore, our AMBER observations of Antares implies that the inhomogeneous, highly temporally variable nature of the outer atmosphere might be common among RSGs.

4. Modeling of the velocity field

The different appearance of the star within the individual CO lines was also detected in Betelgeuse, and it was interpreted as inhomogeneous gas motions in the photosphere and MOLsphere (Papers I and II). To characterize the velocity field using the above reconstructed images of Antares, we applied the

[5] A movie of the spatially resolved spectra across the stellar image is available at http://www.mpifr-bonn.mpg.de/staff/kohnaka

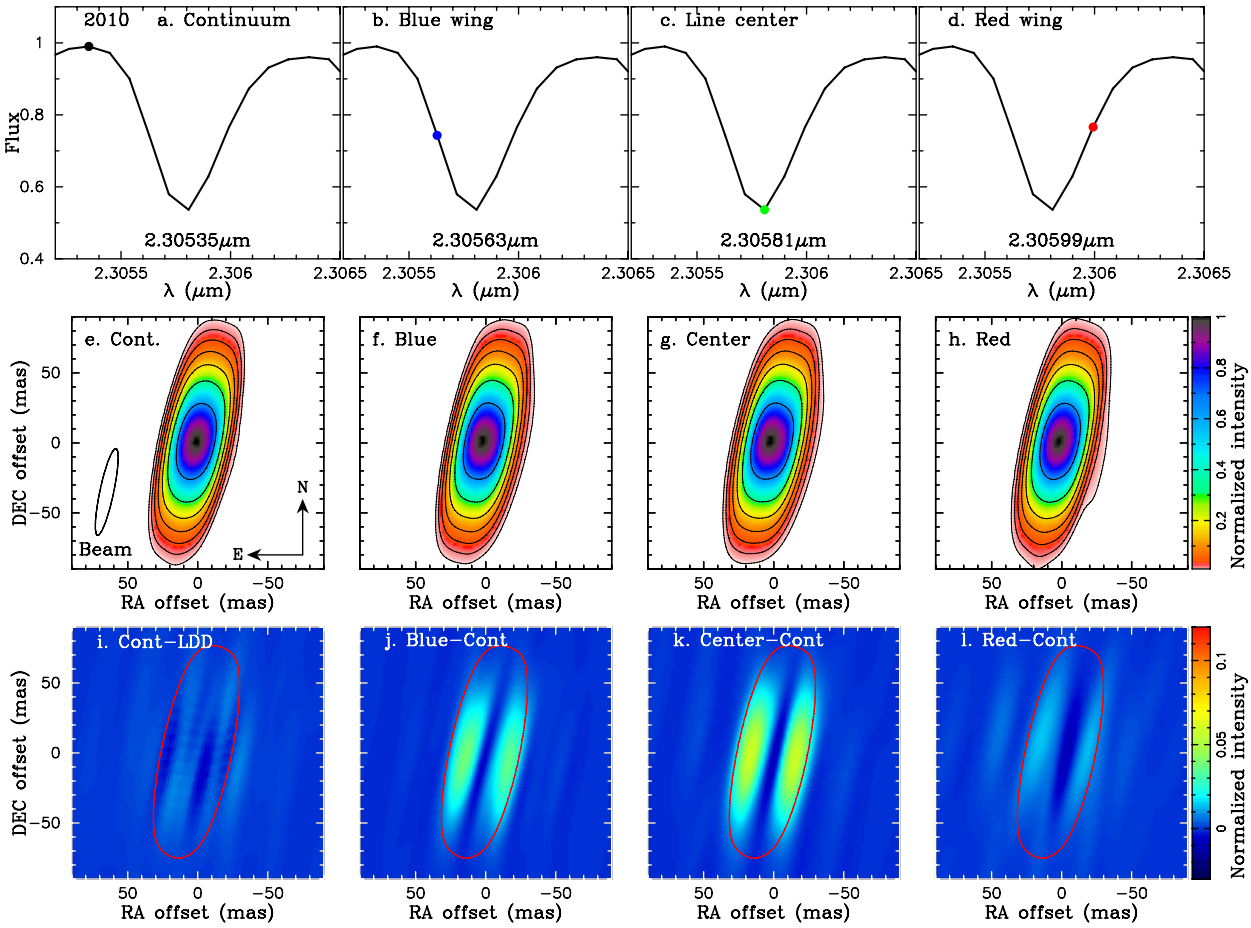

Fig. 7. Reconstructed images of Antares in 2010 shown in the same manner as Fig. 5.

same two-layer model as used for Betelgeuse (see Paper I for details of the model). The star is represented with the blackbody of 3700 K, which is the effective temperature of Antares derived from our continuum visibilities (Sect. 3.2). We represent the CO gas in the photosphere and MOLsphere with an inner and outer layer, respectively. The reason we adopted this two-layer model is that we cannot reproduce the observed CO line spectrum and the CO line images simultaneously with a single layer model. For example, single layer models with CO column densities of 10^{21}–10^{22} cm^{-2} and a radius of ∼1.5 $R_\star$ can roughly explain the observed extended emission in the CO lines. However, these models predict the CO absorption spectrum to be too weak compared to the observations or to appear even in emission, because of the strong extended emission from the layer. This suggests that the inner layer representing the geometrically compact photosphere is necessary to explain the images and spectrum simultaneously.

Each layer is characterized by its radius, CO column density, and temperature. As in Papers I and II, the layers are assumed to be geometrically thin, and the thickness of the layers are fixed to 0.02 $R_\star$. Because this choice is arbitrary, we computed models with larger geometrical thicknesses (up to 0.05 and 0.2 $R_\star$ for the inner and outer layer, respectively) and confirmed that the thickness of the layers does not affect the results of the modeling. Changing the inner layer radius affects the intensity distribution only slightly. The spatial resolution of the current AMBER data is sufficient for constraining the size the MOLsphere (i.e., outer radius) but insufficient for constraining the inner radius. We approximate an inhomogeneous velocity field with a patch (or clump) of CO gas that is moving at a different velocity from the gas in the remaining region.

For the inner CO layer, we adopted the same parameters as for Betelgeuse, because the effective temperature and surface gravity of Antares are similar to those of Betelgeuse ($T_{\rm eff}$ = 3690 K from Paper II and $\log g = -0.3$ from the mass and radius estimated by Harper et al. 2008). We set the radius, temperature, and CO column density of the inner layer to be 1.05 $R_\star$, 2250 K, and 5×10^{22} cm^{-2}, respectively, as in Papers I and II. The radius, temperature, and CO column density of the outer layer, as well as the velocity field, were treated as free parameters, and we assumed the same velocity field for the inner and outer layers. Because the elongated beam of our AMBER observations makes it difficult to know the actual number and shape of stellar spots and the spatial resolution in the North-South direction is low, we assumed only a single patch of CO gas to keep the number of free parameters as small as possible. The model images were spectrally convolved with the spectral resolution of the observed data ($\lambda/\Delta\lambda$ = 8000) and then convolved with the same beam as for the reconstructed images.

Figures 10f–h show the best-fit continuum-subtracted model images derived for the 2009 observations within the same CO line as shown in Fig. 5. A comparison between the observed line profile and that predicted by the model is also shown. This model is characterized by a single large patch (or clump) of CO gas infalling with 2.5 km s^{-1}, which is marked with the dashed circle in the red wing image in Fig. 10d (see also the schematic view in Fig. 12). This CO gas patch or clump produces slightly redshifted absorption, which explains why the intensity

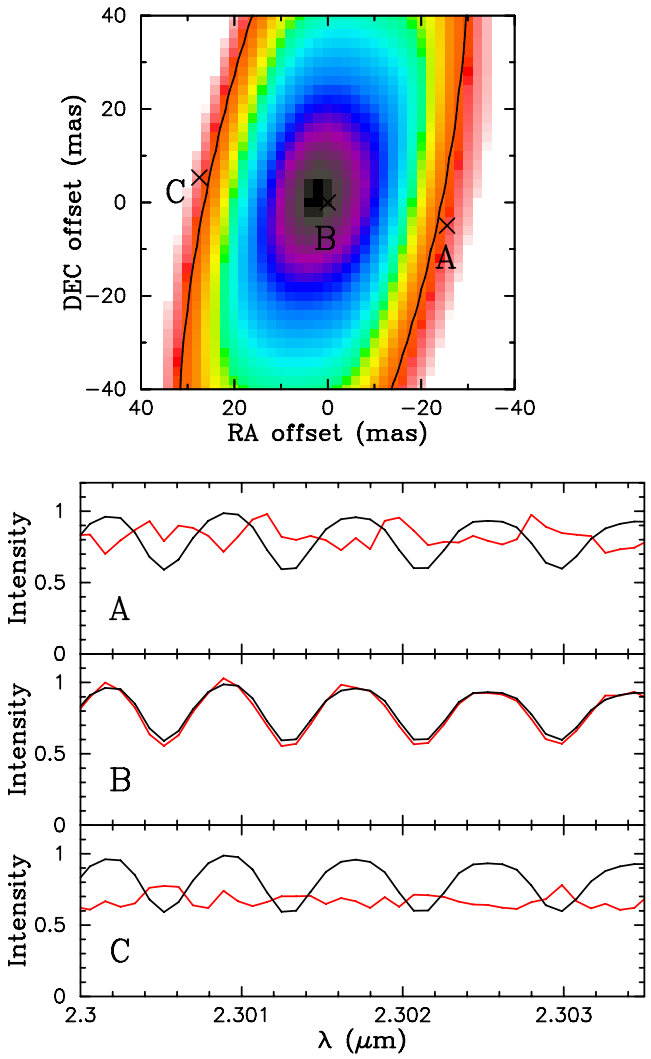

Fig. 8. Spatially resolved spectra obtained in 2010 shown in the same manner as Fig. 6.

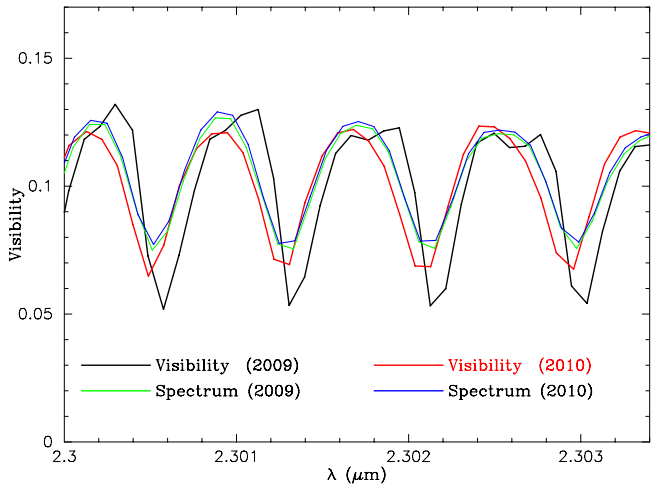

Fig. 9. Comparison of the visibilities observed in 2009 (data set #26, black solid line) and 2010 (data set #107, red solid line). Both visibilities were taken at almost the same projected baseline length (13.9 m) and position angle (84°–85°). The spatially unresolved spectra observed in 2009 and 2010 are also plotted by the green and blue solid lines.

within the patch in the red wing image (Fig. 10d) is lower than in the remaining region. The CO gas outside the patch is moving outward much faster at 25 km s^{-1}, as marked in the line center image in Fig. 10c (see also the schematic view in Fig. 12). The outer CO layer extends to 1.3 $R_\star$ with a temperature of 2000 K and a CO column density of 1×10^{20} cm^{-2}. The extended component observed in the line center and red wing, as well as the absence of it in the blue wing, is reasonably reproduced. From the observed images, the velocity of the CO gas moving inward and outward is constrained to be 0–5 km s^{-1} and 20–30 km s^{-1}, respectively. However, the model predicts the extended component to be too strong, and the observed asymmetry of the extended component (i.e., it extends only to the western side) is not reproduced. The model flux is also too narrow compared to the observed line profile.

A summary of our modeling is given in Table 1. We also computed the reduced χ^2 value for each model in the continuum, blue wing, line center, and red wing from the fit to the observed visibilities and closure phases. The aforementioned differences between the model and the observed images are reflected in the reduced χ^2 values that are much higher than 1. This is presumably due to the simplifications adopted in our model. In particular, we assumed the (radial) column density of CO and temperature in each layer to be constant regardless of the direction with respect to the stellar center and attempted to explain the observed results only by introducing a simplified velocity field. We also assumed a single patch to keep the number of free parameters as small as possible. Therefore, inhomogeneities in the CO density and temperature, as well as multiple patches, may reconcile the disagreement between the observed data and the model. However, our goal is to obtain an approximate picture of the velocity field, and therefore, we refrain from introducing more free parameters, which cannot be well constrained from the present data.

The best-fit continuum-subtracted model images for the 2010 data are shown in Fig. 11. In this model, a large patch of CO gas is moving outward only with 2.5 km s^{-1}, while the CO gas in the remaining region is infalling much faster with 25 km s^{-1} (see also the schematic view in Fig. 12). The patch is so large that it dominates the surface of the star facing toward the observer. The radius and temperature of the outer CO layer are the same as those for the 2009 data, but the CO column density (5×10^{19} cm^{-2}) is smaller than that derived from the 2009 data. The extended component observed in the line center and blue wing is fairly reproduced, and the model image in the red wing shows little trace of the extended component as observed. The model predicts the extended component to be too strong compared to the observed image, and the line profile predicted by the model is also too narrow. However, as mentioned above, this disagreement is likely due to the simplifications adopted in our model. The smaller CO column density of the outer CO layer found for the 2010 data reflects the weaker extended component in 2010 compared to 2009. However, we note that this weaker extended component can also be explained by a model with a smaller radius of 1.2 $R_\star$ and a CO column density of 1×10^{20} cm^{-2} for the outer CO layer. We also found that the models with the upwelling CO gas with 0–5 km s^{-1} and downdrafting gas with 20–30 km s^{-1} can explain the observed data. The uncertainties in the radius, temperature, and CO column density of the outer CO layer are estimated to be ±0.1 $R_\star$, ±200 K, and a factor of 2, respectively.

Comparison between the velocity field obtained from the 2009 and 2010 data reveals that the overall gas motions in the outer atmosphere changed the direction within one year: the

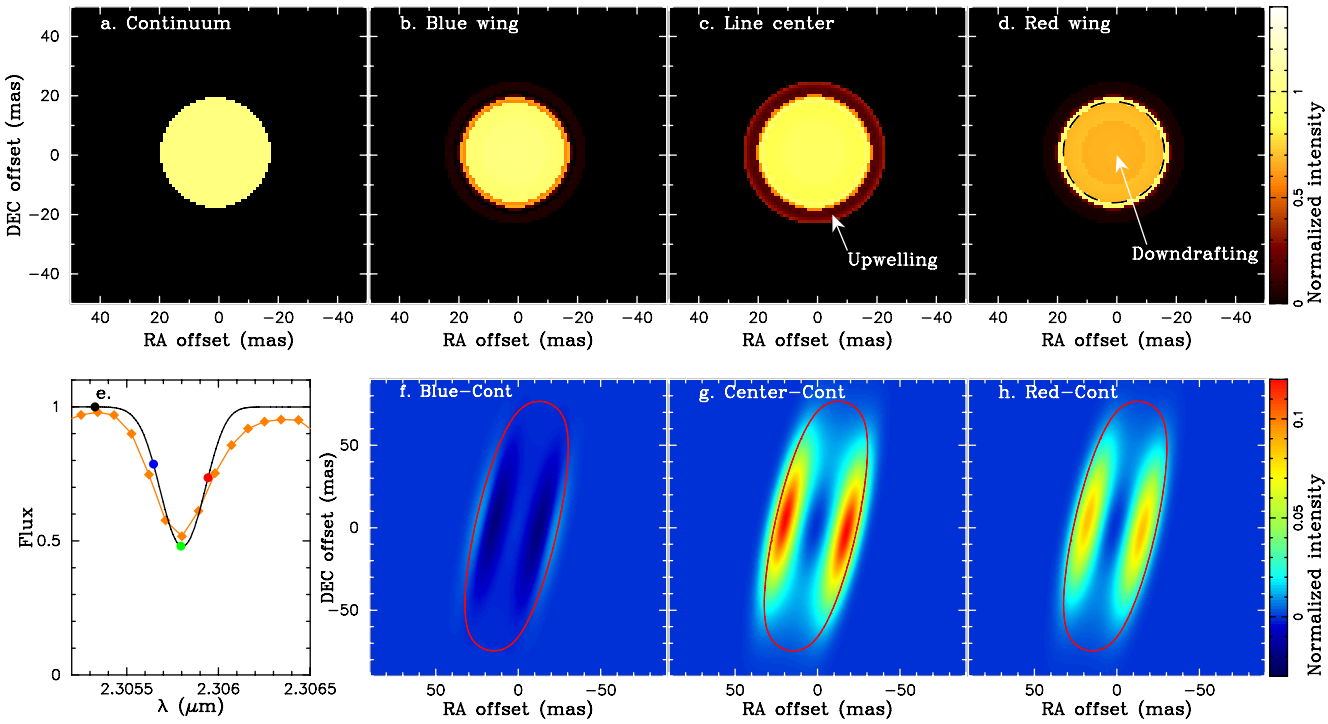

Fig. 10. Best-fit stellar patch model with an inhomogeneous velocity field for Antares observed in 2009. Panels **a)**–**d)** show model images in the continuum, blue wing, line center, and red wing within the same CO line profile as shown in Fig. 5. The wavelengths of these images are marked with black, blue, green, and red dots in panel **e)**, where the observed and model spectra are plotted by the filled diamonds and the black solid line, respectively. Panels **f)**–**h)** show the best-fit continuum-subtracted model images convolved with the same beam as the observed images. Therefore, these model images can be compared to the images shown in Figs. 5j–5l.

Table 1. Parameters of the MOLsphere model with an inhomogeneous velocity field for Antares.

Parameter	Value (2009)	Value (2010)
Inner layer		
CO column density (cm^{-2})	5×10^{22} (fixed)	5×10^{22} (fixed)
Temperature (K)	2250 (fixed)	2250 (fixed)
Radius ($R_\star$)	1.05 (fixed)	1.05 (fixed)
Outer layer		
CO column density (cm^{-2})	1×10^{20} (±0.3 dex)	5×10^{19} (±0.3 dex)
Temperature (K)	2000 ± 200	2000 ± 200
Radius ($R_\star$)	1.3 ± 0.1	1.3 ± 0.1
Velocity field		
Velocity within the patch ($km\,s^{-1}$)	2.5 ± 2.5 (inward)	2.5 ± 2.5 (outward)
Velocity outside the patch ($km\,s^{-1}$)	25 ± 5 (outward)	25 ± 5 (inward)
Stellar patch size (Θ) (°)	60 ± 10	80 ± 10
Stellar patch position (θ, ϕ) (°)	(0–30, 0–360)	(0–30, 0–360)
Reduced χ^2		
Continuum	10.6	18.1
Blue wing	32.6	31.4
Line center	21.0	18.9
Red wing	29.8	20.5

Notes. The definition of the patch size and position is depicted in Fig. 4 of Paper I.

strong upwelling motions were dominant in 2009, while the velocity field in 2010 was dominated by strong downdrafts.

5. Discussion

The characteristics of the velocity field found in Antares are similar to those reported for Betelgeuse in Papers I and II. In both stars, we found CO gas motions with velocity amplitudes of up to 20–30 $km\,s^{-1}$ on a spatial scale larger than the stellar angular radius. Significant time variations in the velocity field have been detected over an interval of one year. The radius, temperature, and density of the outer CO layer derived for Antares are also similar to those in Betelgeuse. Therefore, these inhomogeneous velocity fields in the MOLsphere extending to 1.2–1.5 $R_\star$ might be common among RSGs.

A schematic view of the derived velocity fields in 2009 and 2010 is given in Fig. 12. It is not yet known whether all outwardly moving gas clumps fall back after some time or

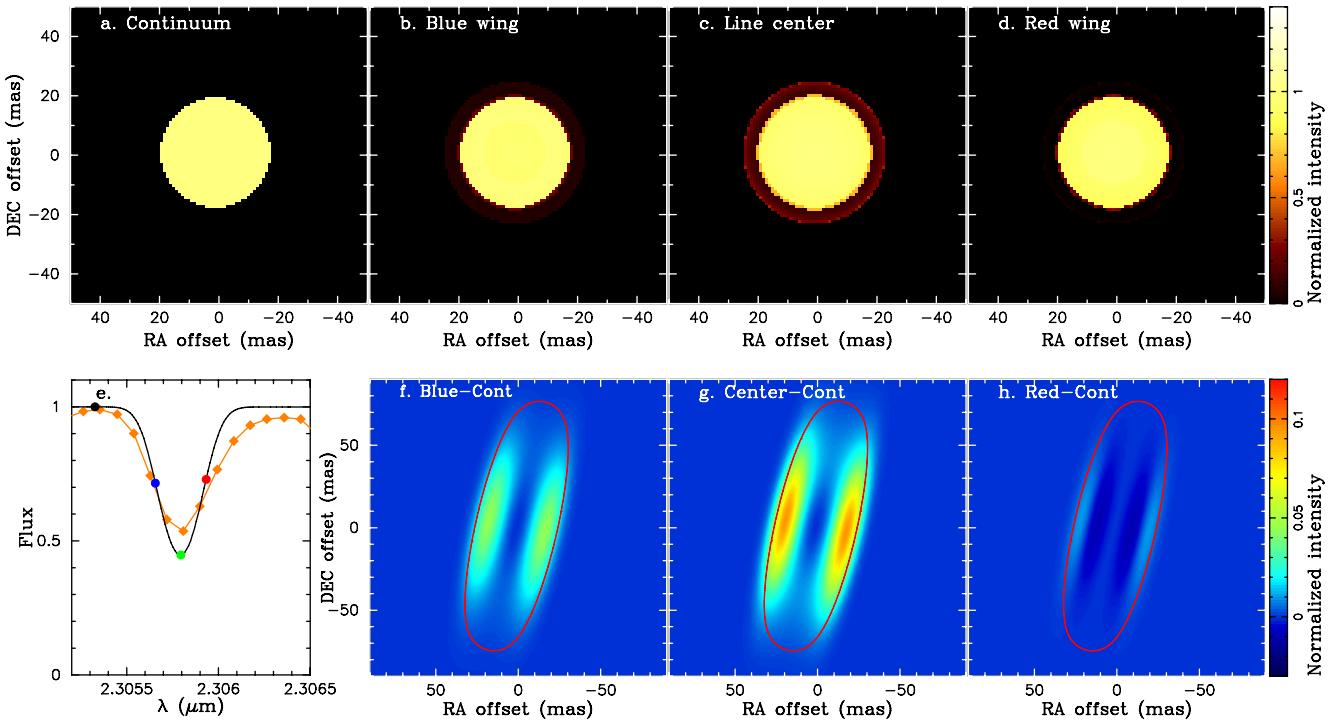

Fig. 11. Best-fit stellar patch model with an inhomogeneous velocity field for Antares observed in 2010, shown in the same manner as Fig. 10. The continuum-subtracted images from the best-fit model, which are shown in panels **f)**–**h)**, are compared to the images shown in Figs. 7j–7l.

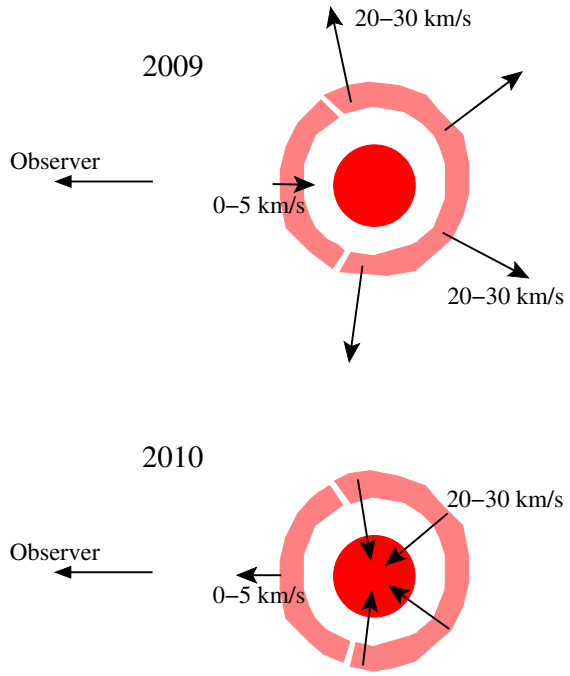

Fig. 12. Schematic view of the velocity fields in Antares derived from our AMBER observations in 2009 and 2010. Only the outer CO layer is drawn for the sake of clarity of the figure, but the velocity field of the inner CO layer was assumed to be the same as in the outer layer. The images are not to scale.

they are further accelerated outward. If we assume that the inhomogeneous CO gas motions in Antares are ballistic, the CO gas moving outward with 20–30 km s^{-1} seen at 1.3–1.4 $R_\star$ in April 2009 reaches a maximum height of 1.45–1.60 $R_\star$ in 2–3 months and falls back to the original height in another 2–3 months. Likewise, if we assume that the CO gas infalling fast at 20–30 km s^{-1} seen in 2010 is falling back from some height with an initial velocity of zero, it is estimated to have traveled from 1.45–1.60 $R_\star$ over 2–3 months. On the other hand, the CO gas moving inward at only 0–5 km s^{-1} (2009) or outward (2010) may represent a clump that has traveled from a deeper layer and is near the maximum height, at which the velocity is zero. In this case, the clump is estimated to have traveled from ∼1.2 $R_\star$ with an initial velocity of 20–30 km s^{-1} over approximately two months. This means that multi-epoch AMBER observations over 2–6 months would be useful for probing whether the outwardly moving gas clump falls back or it is accelerated outward further.

The physical mechanism responsible for the formation of the MOLsphere and the inhomogeneous gas motions in this region is still unclear. The upwelling and downdrafting motions are reminiscent of convection, which may levitate the gas to form the MOLsphere. For example, Lim et al. (1998) suggest that convection could lift the photospheric material into the extended atmosphere. If convection alone is responsible for the formation of the MOLsphere, 3D convection simulations should predict the density consistent with the observationally derived values at the location of the MOLsphere (1.2–1.4 $R_\star$).

Given that the current 3D convection simulations cover up to 8–9 $R_\star$, it is possible to carry out this comparison. One of the 3D models of Chiavassa et al. (2011), which is closest to Antares or Betelgeuse, shows that the density at 1.2 $R_\star$ ranges between 10^{-20} and 10^{-25} g cm^{-3} (see their Fig. 4). On the other hand, we can estimate the gas density in the MOLsphere as follows. While we adopted the geometrical thickness of 0.02 $R_\star$ for the outer CO layer representing the MOLsphere, the inner radius of the MOLsphere is not observationally constrained. Therefore, we estimated a lower limit on the CO density by dividing the CO column density with the geometrical thickness defined by the outer radius of the MOLsphere (i.e., geometrical

thickness = 0.2–0.4 $R_\star$). If we assume chemical equilibrium in the MOLsphere, we can estimate the gas density from the CO density and the temperature of the MOLsphere (2000 K). The derived gas density is $\sim 10^{-14}$ cm^{-3}, which is higher than the values predicted by the 3D convection model by six to eleven orders of magnitude. The analysis of line profiles in Antares by Gray & Pugh (2012) also implies that convective cells penetrate only the lower portion of the photosphere, although it is not straightforward to convert the radial velocities derived from spatially unresolved spectra to the actual velocity field. Therefore, at the moment, convection alone is unlikely to explain the formation of the MOLsphere and the inhomogeneous gas motions. However, it remains to be tested whether the combination of convection and some other mechanism (e.g., radiation pressure on molecules and atoms or scattering on dust grains) can explain the formation of the MOLsphere and the mass loss in RSGs.

Another possible mechanism is the propagation of Alfvén waves. Magnetic fields have been detected in Betelgeuse (Aurière et al. 2010). While Grunhut et al. (2010) detected no magnetic fields in Antares, this can be due to the insufficient S/N as they themselves note. Therefore, future observations with a better S/N may reveal magnetic fields in more RSGs including Antares, and the magnetohydrodynamical (MHD) wave propagation remains a possible process to explain the formation of the MOLsphere and the inhomogeneous gas motions. However, the currently available MHD model by Airapetian et al. (2000) deals with the stellar winds from the chromosphere and does not include the MOLsphere. The recent magneto-rotator model by Thirumalai & Heyl (2012) represents an interesting alternative for the RSG mass loss, although their model is still stationary and does not include the chromosphere. The inclusion of a proper treatment of the time-dependent, multicomponent nature (chromosphere and MOLsphere) would be crucial for testing whether or not the MHD process with or without rotation is responsible for the formation of the MOLsphere and the inhomogeneous gas motions.

While the presence of the MOLsphere is confirmed by the IR interferometric imaging of Antares and Betelgeuse in the individual CO lines, there are still problems with the MOLsphere, as mentioned in Ohnaka et al. (2012). The additional TiO absorption originating in the MOLsphere makes the TiO bands too strong compared to the observed spectra of RSGs (Hron et al. 2010). As Ohnaka et al. (2012) suggest, the scattering due to TiO molecules may reconcile the above problem, because the line formation by scattering can be important for electronic transitions such as the TiO bands in the visible. Another problem is that the current MOLsphere models cannot explain the high resolution 12 μm spectra of H_2O lines (Ryde et al. 2006). Recently, Lambert et al. (2013) suggest the importance of NLTE effects in the formation of these H_2O lines. Therefore, modeling with the scattering of molecules and NLTE effects taken into account is necessary for a comprehensive understanding of the MOLsphere.

6. Concluding remarks

We have presented high spectral resolution aperture-synthesis imaging of Antares at two epochs with VLTI/AMBER. With the stellar surface spatially resolved with AMBER's high spatial resolution, AMBER's high spectral resolution has enabled us to derive the kinematical information at different positions over the surface of the star. The reconstructed images obtained at the first epoch (April 2009) reveal an asymmetrically extended component (MOLsphere) in the red wing and line center of the individual lines, while the image in the blue wing shows little trace of the extended component. At the second epoch (April 2010), the extended component appears in the blue wing and line center, and the red wing image does not exhibit the extended component. We have also found that the extended component became weaker in 2010. These results can be interpreted as a significant time variation in the atmospheric dynamics.

Our modeling suggests that the velocity field in the MOLsphere in 2009 is characterized by a large patch or clump of CO gas infalling at only 0–5 km s^{-1} with the CO gas in the remaining region moving outwardly much faster at 20–30 km s^{-1}. The data observed in 2010 are explained by a model in which a large patch of CO gas moving outwardly at 0–5 km s^{-1} and the CO gas in the remaining region is infalling faster at 20−30 km s^{-1}. Our modeling also shows that the MOLsphere is extended to 1.2–1.4 $R_\star$ with column densities of 5×10^{19}–1×10^{20} cm^{-2} and a temperature of ∼2000 K. These properties of the MOLsphere of Antares, as well as the velocity field, are very similar to those derived for Betelgeuse. Therefore, the inhomogeneous gas motions in the MOLsphere extending to 1.2–1.5 $R_\star$ might be common among RSGs.

The origin of the detected gas motions is not clear yet. To understand the physical mechanism responsible for the dynamics and formation of the MOLsphere, it is necessary to spatially resolve the dynamics at different heights from the deep photosphere to the outer atmosphere. Similar AMBER observations for different atomic and molecular lines would make this possible. For example, weak atomic lines such as Ti, Na, and Ca would be useful for probing the dynamics in the deep photospheric layers. Moreover, it is essential to obtain images with better *uv* coverage. This is now feasible with more telescope configurations appropriate for the aperture-synthesis imaging available at the VLTI.

Acknowledgements. We thank the ESO VLTI team for supporting our AMBER observations. We are also grateful to Eric Thiébaut, who makes his image reconstruction software MiRA publicly available. NSO/Kitt Peak FTS data on the Earth's telluric features were produced by NSF/NOAO.

References

Airapetian, V. S., Ofman, L., Robinson, R. D., Carpenter, K., & Davila, J. 2000, ApJ, 528, 965
Aurière, M., Donati, J.-F., Konstantinova-Antova, R., et al. 2010, A&A, 516, L2
Bloemhof, E. E., & Danen, R. M. 1995, ApJ, 440, L93
Bloemhof, E. E., Townes, C. H., & Vanderwyck, A. H. B. 1984, ApJ, 276, L21
Braun, K., Baade, R., Reimers, D., & Hagen, H.-J. 2012, A&A, 546, A3
Chiavassa, A., Plez, B., Josselin, E., & Freytag, B. 2009, A&A, 506, 1351
Chiavassa, A., Freytag, B., Masseron, T., & Plez, B. 2011, A&A, 535, A22
Ducati, J. R. 2002, Catalogue of Stellar Photometry in Johnson's 11-color system
Efron, B., & Tibshirani, R. J. 1993, An Introduction to the Bootstrap (New York: Chapman & Hall)
Elias, J. H., Frogel, J. A., & Humphreys, R. M. 1985, ApJS, 57, 91
Ekström, S., Georgy, C., Eggenberger, P., et al. 2012, A&A, 537, A146
Gilliland, R. L., & Dupree, A. K. 1996, ApJ, 463, L29
Gontscharov, G. A. 2006, Astron. Lett., 32, 759
Gray, D., & Pugh, T. 2012, AJ, 143, 92
Grunhut, J. H., Wade, G. A., Hanes, D. A., & Alecian, E. 2010, MNRAS, 408, 2290
Harper, G. M. 2010, Hot and Cool: Bridging Gaps in Massive Star Evolution, ASP Conf. Ser., 425, 152
Harper, G. M., & Brown, A. 2001, ApJ, 551, 1073
Harper, G. M., Brown, A., & Guinan, E. 2008, AJ, 135, 1430
Haubois, X., Perrin, G., Lacour, S., et al. 2009, A&A, 508, 923
Hebden, J. C., Eckart, A., & Keith Hege, E. 1987, ApJ, 314, 690
Hestroffer, D. 1997, A&A, 327, 199
Hron, J., Aringer, B., & Paladini, C. 2010, Poster presentation at The Origin and Fate of the Sun: Evolution of Solar-mass Stars Observed with High Angular Resolution, http://www.eso.org/sci/meetings/2010/stars2010/Presentations/P-hron_molsphere-poster.pdf

Jennings, D. E., & Sada, P. V. 1998, Science, 279, 844
Kervella, P., Thévenin, F., Ségransan, D., et al. 2003, A&A, 404, 1087
Kervella, P., Verhoelst, T., Ridgway, S. T., et al. 2009, A&A, 504, 115
Kervella, P., Perrin, G., Chiavassa, A., et al. 2011, A&A, 531, A117
Lambert, J., Josselin, E., Ryde, N., & Faure, A. 2013, Proceedings of Betelgeuse Workshop 2012, The physics of Red Supergiants: recent advances and open questions, EAS Publ. Ser., in press (http://arxiv.org/abs/1304.4111)
Lee, T. A. 1970, PASP, 82, 765
Levesque, E. M., Massey, P., Olsen, K. A., Plez, B., & Josselin, E. 2005, ApJ, 628, 973
Lim, J., Carilli, C., White, S. M., Beasley, A. J., & Marson, R. G. 1998, Nature, 392, 575
Low, F. J., Johnson, H. L., Kleinmann, D. E., Latham, A. S., & Geisel, S. L. 1970, ApJ, 160, 531
Marsh, K. A., Bloemhof, E. E., Koerner, D. W., & Ressler, M. E. 2001, ApJ, 548, 861
Monnier, J. D., Geballe, T., & Danchi, W. C. 1998, ApJ, 502, 833
Ohnaka, K. 2013, Proceedings of Betelgeuse Workshop 2012, The physics of Red Supergiants: recent advances and open questions, EAS Publ. Ser., 60, 121
Ohnaka, K., Hofmann, K.-H., Benisty, M., et al. 2009, A&A, 503, 183 (Paper I)
Ohnaka, K., Weigelt, G., Millour, F., et al. 2011, A&A, 529, A163 (Paper II)
Ohnaka, K., Hofmann, K.-H., Schertl, D., et al. 2012, A&A, 537, A53
Pecaut, M. J., Mamajek, E. E., & Bubar, E. J. 2012, ApJ, 746, 154
Petrov, R. G., Malbet, F., Weigelt, G., et al. 2007, A&A, 464, 1
Price, S. D., Smith, B. J., Kuchar, T. A., Mizuno, D. R., & Kraemer, K. E. 2010, ApJS, 190, 203
Richichi, A., & Lisi, F. 1990, A&A, 230, 355
Ryde, N., Harper, G. M., Richter, M. J., Greathouse, T. K., & Lacy, J. H. 2006, ApJ, 637, 1040
Savage, B. D., & Mathis, J. S. 1979, ARA&A, 17, 73
Skrutskie, M. F., Cutri, R. M., Stiening, R., et al. 2006, AJ, 131, 1163
Smartt, S. J., Eldridge, J. J., Crockett, R. M., & Maund, J. R. 2009, MNRAS, 395, 1409
Tatulli, E., Millour, F., Chelli, A., et al. 2007, A&A, 464, 29
Thiébaut, E. 2008, SPIE Procs., 7013, 70131I
Thirumalai, A., & Heyl, J. S. 2012, MNRAS, 422, 1272
Tsuji, T. 2000a, ApJ, 538, 801
Tsuji, T. 2000b, ApJ, 540, L99
Tuthill, P. G., Haniff, C. A., & Baldwin, J. E. 1997, MNRAS, 285, 529
van Leeuwen, F. 2007, A&A, 474, 653
Verhoelst, T., Van der Zypern, N., Hony, S., et al. 2009, A&A, 498, 127
Wallace, L., & Hinkle, K. H. 1996, ApJS, 107, 312
White, N. M., Kreidl, T. J., & Goldberg, L. 1982, ApJ, 254, 670

Pages 14 to 18 are available in the electronic edition of the journal at http://www.aanda.org

Appendix A: Summary of AMBER observations

Our AMBER observations of Antares are summarized in Tables A.1 and A.2.

Table A.1. Log of AMBER observations of Antares and the calibrator α Cen A in April 2009 with the E0-G0-H0 (16-32-48 m) baseline configuration.

#	t_{obs} (UTC)	B_p (m)	PA (°)	s (″)	τ_0 (ms)	NDIT	#	t_{obs} (UTC)	B_p (m)	PA (°)	s (″)	τ_0 (ms)	NDIT
Antares													
2009 Apr. 24							2009 Apr. 25						
1	05:14:38	30.06/15.04/45.09	58/ 58/ 58	0.65	4.2	500	36	05:01:04	29.67/14.84/44.51	56/ 56/ 56	0.52	5.0	200
2	05:16:57	30.14/15.08/45.22	58/ 58/ 58	0.79	3.6	500	37	05:02:05	29.71/14.86/44.57	56/ 56/ 56	0.53	4.9	200
3	05:19:17	30.22/15.12/45.34	59/ 59/ 59	0.87	3.1	500	38	05:08:10	29.96/14.99/44.96	57/ 57/ 57	0.51	5.1	500
4	05:21:36	30.30/15.16/45.46	59/ 59/ 59	0.90	3.1	500	39	05:10:30	30.05/15.03/45.08	58/ 58/ 58	0.54	4.8	500
5	05:23:56	30.38/15.20/45.58	59/ 59/ 59	1.02	2.6	500	40	05:12:49	30.13/15.08/45.21	58/ 58/ 58	0.55	4.6	500
6	06:09:54	31.59/15.80/47.39	66/ 66/ 66	0.56	5.4	500	41	05:15:08	30.21/15.12/45.33	59/ 58/ 59	0.57	4.5	500
7	06:12:13	31.63/15.83/47.45	66/ 66/ 66	0.54	5.0	500	42	05:17:28	30.30/15.16/45.45	59/ 59/ 59	0.60	4.2	500
8	06:14:32	31.67/15.84/47.51	66/ 66/ 66	0.52	5.1	500	43	06:00:05	31.47/15.75/47.22	65/ 65/ 65	0.70	3.7	500
9	06:16:52	31.70/15.86/47.57	66/ 66/ 66	0.54	4.9	500	44	06:02:25	31.52/15.77/47.29	65/ 65/ 65	0.71	3.6	500
10	06:19:11	31.74/15.88/47.62	67/ 67/ 67	0.57	4.6	500	45	06:04:45	31.57/15.79/47.36	65/ 65/ 65	0.62	4.1	500
11	07:10:49	31.92/15.97/47.90	73/ 73/ 73	0.41	6.2	500	46	06:07:04	31.61/15.81/47.42	66/ 66/ 66	0.60	4.2	500
12	07:13:08	31.90/15.96/47.87	73/ 73/ 73	0.38	6.7	500	47	06:09:24	31.65/15.83/47.48	66/ 66/ 66	0.61	4.1	500
13	07:15:27	31.88/15.95/47.84	73/ 73/ 73	0.39	6.6	500	48	07:32:32	31.58/15.80/47.38	75/ 75/ 75	0.50	6.0	500
14	07:17:47	31.86/15.94/47.80	73/ 73/ 73	0.41	6.2	500	49	07:34:51	31.53/15.78/47.31	76/ 76/ 76	0.50	6.0	500
15	07:20:06	31.83/15.93/47.76	74/ 74/ 74	0.39	6.6	500	50	07:37:11	31.48/15.75/47.24	76/ 76/ 76	0.50	6.0	500
16	07:49:43	31.28/15.65/46.93	77/ 77/ 77	0.53	4.8	500	51	07:39:30	31.43/15.73/47.16	76/ 76/ 76	0.52	5.9	500
17	07:52:02	31.22/15.62/46.84	77/ 77/ 77	0.46	5.5	500	52	07:41:50	31.38/15.70/47.08	76/ 76/ 76	0.54	5.7	500
18	07:54:22	31.16/15.59/46.75	77/ 77/ 77	0.44	5.7	500	53	08:18:31	30.19/15.11/45.30	80/ 80/ 80	0.52	6.3	500
19	07:56:42	31.09/15.56/46.65	77/ 77/ 77	0.42	5.9	500	54	08:20:50	30.10/15.06/45.16	80/ 80/ 80	0.56	5.9	500
20	07:59:02	31.02/15.52/46.54	78/ 78/ 78	0.43	5.8	500	55	08:23:10	30.00/15.01/45.01	80/ 80/ 80	0.54	6.3	500
21	08:29:57	29.87/14.95/44.82	81/ 81/ 81	0.54	4.6	500	56	08:25:29	29.90/14.96/44.86	81/ 81/ 81	0.49	6.9	500
22	08:32:17	29.77/14.90/44.67	81/ 81/ 81	0.49	5.1	500	57	08:27:48	29.79/14.91/44.70	81/ 81/ 81	0.46	7.3	500
23	08:34:37	29.66/14.84/44.51	81/ 81/ 81	0.49	5.1	500	58	09:20:25	–/–/40.22	–/–/ 86	0.67	5.8	500
24	08:36:56	29.55/14.79/44.34	81/ 81/ 81	0.50	5.0	500	59	09:22:44	–/–/39.98	–/–/ 86	0.65	5.9	500
25	08:39:15	29.44/14.73/44.18	82/ 82/ 82	0.49	5.1	500	60	09:25:04	–/–/39.74	–/–/ 86	0.64	6.1	500
26	09:10:08	27.73/13.88/41.61	85/ 85/ 85	0.40	6.2	500	61	09:27:23	–/–/39.49	–/–/ 87	0.67	5.9	500
27	09:12:28	27.59/13.81/41.39	85/ 85/ 85	0.38	6.6	500	62	09:29:42	–/–/39.24	–/–/ 87	0.71	5.5	500
28	09:14:47	27.44/13.73/41.17	85/ 85/ 85	0.37	6.7	500	63	10:24:35	21.68/10.85/32.54	93/ 93/ 93	0.56	8.1	200
29	09:17:06	27.29/13.66/40.95	85/ 85/ 85	0.38	6.6	500	64	10:25:37	21.59/10.80/32.39	93/ 93/ 93	0.59	7.8	200
30	09:19:27	27.14/13.58/40.72	85/ 85/ 85	0.39	6.4	500	65	10:26:39	21.49/10.76/32.25	93/ 93/ 93	0.60	7.6	200
31	09:48:22	25.05/12.54/37.59	88/ 88/ 88	0.49	5.0	500							
32	09:50:41	24.87/12.45/37.31	89/ 89/ 89	0.53	4.7	500							
33	09:53:00	24.68/12.35/37.04	89/ 89/ 89	0.55	4.5	500							
34	09:55:19	24.50/12.26/36.76	89/ 89/ 89	0.56	4.5	500							
35	09:57:39	24.31/12.17/36.48	89/ 89/ 89	0.53	4.7	500							
α Cen A													
2009 Apr. 24							2009 Apr. 25						
C1	05:35:10	30.98/15.50/46.48	81/ 81/ 81	0.74	3.8	2500	C6	05:30:35	30.99/15.51/46.49	80/ 80/ 80	0.65	4.0	2500
C2	06:48:04	29.38/14.70/44.07	96/ 96/ 96	0.77	3.3	2500	C7	06:23:17	29.91/14.97/44.87	92/ 92/ 92	0.60	4.2	2500
C3	07:31:50	28.10/14.06/42.16	107/107/107	0.40	6.4	2500	C8	07:56:55	27.16/13.59/40.75	114/114/114	0.43	7.3	2500
C4	08:10:33	26.84/13.43/40.27	116/116/116	0.43	5.8	2500	C9	08:41:46	25.66/12.84/38.50	125/125/125	0.35	9.7	2500
C5	08:51:55	25.46/12.74/38.20	127/127/127	0.51	5.0	2500	C10	09:45:10	–/–/35.57	–/–/144	0.61	6.8	2500

Notes. The seeing (s) and the coherence time (τ_0) are in the visible.

Table A.2. Log of AMBER observations of Antares and the calibrators α Cen A and α Cen B in April 2010.

#	t_{obs} (UTC)	B_p (m)	PA (°)	s (″)	τ_0 (ms)	NDIT	#	t_{obs} (UTC)	B_p (m)	PA (°)	s (″)	τ_0 (ms)	NDIT
Antares													
2010 Apr. 10							2010 Apr. 11						
66	06:19:19	45.55/15.19/30.36	59/ 59/ 59	1.02	47.1	500	89	05:47:04	43.95/14.66/29.30	55/55/55	0.78	30.5	500
67	06:21:30	45.66/15.23/30.44	59/ 59/ 59	0.97	31.3	500	90	05:49:16	44.09/14.70/29.39	55/55/55	0.74	23.9	500
68	06:23:41	45.77/15.26/30.51	60/ 60/ 60	0.99	28.1	500	91	05:51:27	44.22/14.75/29.47	55/55/55	0.75	23.1	500
69	06:25:51	45.88/15.30/30.58	60/ 60/ 60	1.11	25.9	500	92	05:53:37	44.35/14.79/29.56	56/56/56	0.67	30.7	500
70	06:28:02	45.98/15.33/30.65	60/ 60/ 60	1.07	29.7	500	93	05:55:48	44.48/14.83/29.65	56/56/56	0.69	27.5	500
71	07:16:22	47.64/15.89/31.76	67/ 67/ 67	0.83	21.8	500	94	06:34:20	46.44/15.49/30.95	62/62/62	0.72	17.1	500
72	07:18:32	47.69/15.90/31.78	67/ 67/ 67	0.81	21.8	500	95	06:36:31	46.53/15.52/31.01	62/62/62	0.69	17.8	500
73	07:20:43	47.73/15.92/31.81	67/ 67/ 67	0.78	20.5	500	96	06:38:41	46.61/15.54/31.07	62/62/62	0.68	18.2	500
74	07:22:53	47.77/15.93/31.84	68/ 68/ 68	0.84	17.6	500	97	06:40:52	46.70/15.57/31.13	63/63/63	0.66	19.5	500
75	07:25:03	47.80/15.94/31.86	68/ 68/ 68	0.85	18.0	500	98	06:43:03	46.78/15.60/31.18	63/63/63	0.67	20.3	500
76	08:44:42	46.97/15.66/31.30	77/ 77/ 77	0.68	15.4	500	99	07:20:36	47.79/15.94/31.86	68/68/68	0.70	34.6	500
77	08:46:53	46.88/15.64/31.25	77/ 77/ 77	0.66	15.7	500	100	09:21:33	65.11/54.08/14.96	118/128/81	0.75	20.6	500
78	08:49:03	46.80/15.61/31.19	77/ 77/ 77	0.69	15.0	500	101	09:23:43	64.94/53.97/14.91	119/128/81	0.74	21.7	500
79	08:51:14	46.71/15.58/31.13	77/ 77/ 77	0.71	14.8	500	102	09:25:54	64.77/53.85/14.86	119/129/81	0.76	23.1	500
80	08:53:25	46.61/15.55/31.07	77/ 77/ 77	0.69	14.8	500	103	09:28:05	64.60/53.74/14.81	119/129/81	0.78	23.4	500
81	09:36:33	44.08/14.70/29.38	82/ 82/ 82	0.70	15.2	500	104	09:30:15	64.42/53.62/14.76	120/129/81	0.78	23.4	500
82	09:38:45	43.92/14.65/29.27	82/ 82/ 82	0.85	12.8	500	105	09:56:49	62.04/52.07/14.04	124/134/84	0.71	30.4	500
83	09:40:55	43.75/14.59/29.16	82/ 82/ 82	0.88	12.8	500	106	09:58:59	61.83/51.93/13.98	124/134/84	0.68	28.1	500
84	09:43:06	43.58/14.54/29.05	82/ 82/ 82	0.85	12.7	500	107	10:01:09	61.61/51.79/13.91	125/135/84	0.71	27.2	500
85	09:45:17	43.41/14.48/28.93	82/ 82/ 83	0.91	10.3	500	108	10:03:19	61.40/51.66/13.84	125/135/85	0.81	26.8	500
86	10:19:23	40.32/13.45/26.87	86/ 86/ 86	0.64	27.5	500	109	10:05:31	61.18/51.52/13.77	126/136/85	0.90	26.3	500
87	10:21:34	40.09/13.37/26.72	86/ 86/ 86	0.68	26.1	500							
88	10:23:45	39.87/13.30/26.57	86/ 86/ 86	0.72	24.6	500							
α Cen A													
2010 Apr. 10							2010 Apr. 11						
C11	05:57:07	47.21/15.74/31.46	73/ 73/ 73	0.85	35.2	2500	C16	05:21:35	47.66/15.89/31.77	67/ 67/ 67	–99.99	24.5	2500
C12	06:55:08	45.81/15.28/30.53	86/ 86/ 86	0.78	30.6	2500	C17	06:12:28	46.82/15.61/31.21	77/ 77/ 77	0.67	20.1	2500
C13	07:46:14	43.98/14.67/29.32	97/ 97/ 97	0.67	21.5	2500	C18	07:00:07	45.53/15.18/30.35	88/ 88/ 88	0.58	31.5	2500
C14	09:16:12	39.78/13.27/26.52	119/118/119	0.71	13.8	2500							
C15	10:02:42	37.47/12.49/24.97	131/131/131	0.69	13.8	2500							
α Cen B													
2010 Apr. 10							2010 Apr. 11						
							C19	08:58:05	68.07/56.52/13.50	143/150/115	0.54	32.9	2500

Notes. The data sets #66–99 and C#11–C#18 were taken with the E0-G0-H0 (16-32-48 m) telescope configuration, while the data sets #100–109 and C#19 were taken with the E0-G0-I1 (16-57-69m) configuration. The seeing (s) and the coherence time (τ_0) are in the visible.

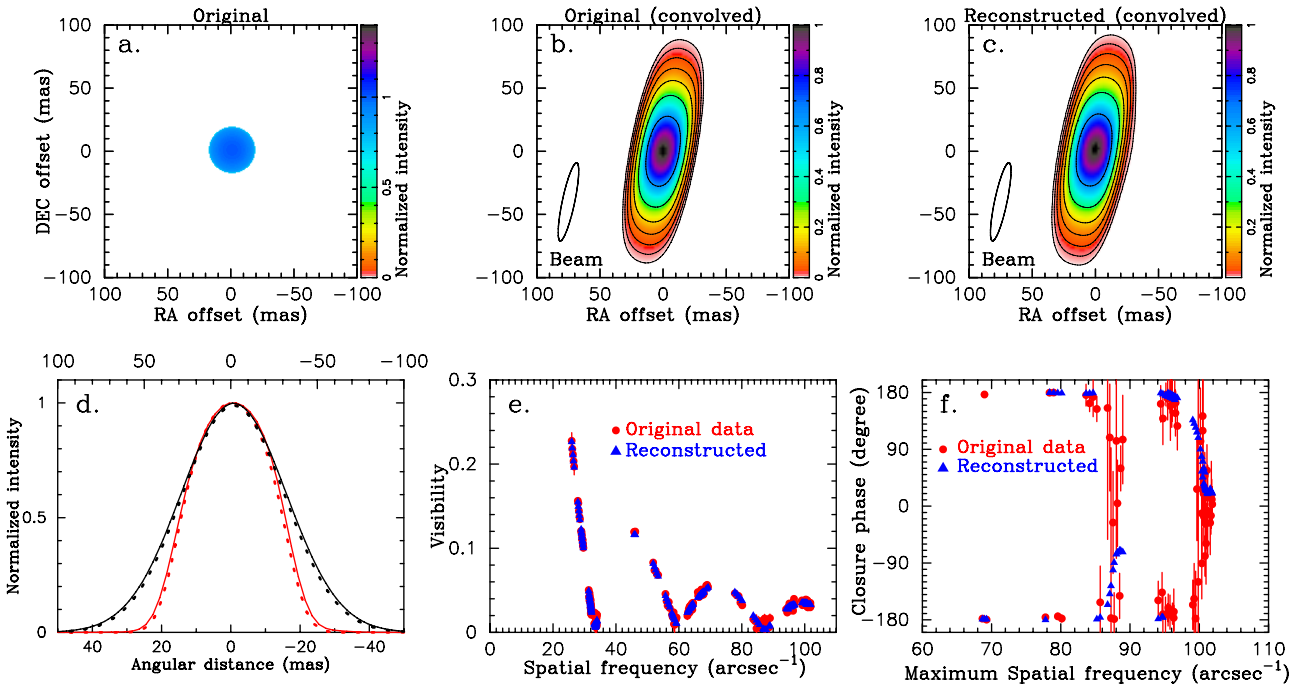

Fig. B.1. Image reconstruction from the simulated data for a limb-darkened disk with the parameters derived from the 2009 data. **a)** Original image. **b)** Original image after convolving with the Gaussian beam with 9.8 × 63.2 mas. **c)** Reconstructed image after convolving with the beam. **d)** The intensity profiles of the original image are plotted by the red dotted line (along the minor axis) and the black dotted line (along the major axis). The intensity profiles of the reconstructed images are plotted by the red solid line (along the minor axis) and black solid line (along the major axis). The abscissa for the intensity profiles along the major axis is shown at the top of the panel. **e)** Comparison between the visibilities generated from the original image (filled dots) and those from the reconstructed image (triangles). **f)** Comparison between the CPs generated from the original image (filled dots) and those from the reconstructed image (triangles).

Appendix B: Image reconstruction of simulated data

We generated interferometric data (visibility amplitudes and closure phases) from simulated stellar images by sampling at the same *uv* points as our AMBER observations. The image reconstruction from these simulated interferometric data allows us to find the appropriate parameters (such as the initial model, prior, and regularization scheme) that can restore the original images correctly.

For our data on Antares, we tested the image reconstruction for a limb-darkened disk with the angular diameter and the limb-darkening parameter derived for the 2009 data and a uniform disk with surface inhomogeneities and an extended component. The simulated interferometric data were generated using a program developed by one of the authors (Hofmann) as follows. For each telescope triplet, we simulated two-telescope interferograms corresponding to the three baseline vectors for a given object (e.g., limb-darkened stellar disk or spotted star). The simulated interferograms were degraded by the atmospheric piston, photon noise, sky background, and detector noise. From ∼1000 simulated two-telescope interferograms on each baseline, the average power spectrum and bispectrum were calculated. The subtraction of the noise bias terms and calibration with an unresolved calibrator star yielded the calibrated visibilities and closure phases for the simulated object. The amount of noise in the simulated interferograms was chosen to obtain approximately the same errors as in the AMBER measurements of Antares.

The reconstructed images were convolved with the clean beam, which was determined in the following manner. The spatial resolution in the direction of the *uv* points with the longest baseline length ($B_{\rm max}$) is given by $\lambda/B_{\rm max}$ = 9.8 mas. However, the sparse *uv* coverage shown in Fig. 1 leads to a strongly elongated beam. We fitted the central peak of the dirty beam with a 2D Gaussian and derived the ratio between the major and minor axes and the position angle. The beam defined in this manner is narrower than that given by $\lambda/B_{\rm max}$, because of the lack of data at very short baselines. Therefore, we scaled the major and minor axes of this Gaussian beam so that the beam size along the minor axis matches the resolution given by $\lambda/B_{\rm max}$. The final clean beam for the *uv* coverage obtained in 2009 is a 2D Gaussian with 9.8 × 63.2 mas (FWHM) with the major axis at a position angle of −12°.

The results of the image reconstruction of two sets of simulated data are shown in Figs. B.1 and B.2. The reconstructed images agree reasonably well with the original image after convolving with the beam. These tests show that the uniform-disk initial model with angular diameters of 36–37 mas and the same prior as used in Paper II are appropriate for the image reconstruction from our AMBER data of Antares. The prior is given by

$$Pr(r) = \frac{1}{e^{(r-r_{\rm p})/\varepsilon_{\rm p}} + 1},$$

where r is the radial coordinate in mas, and $r_{\rm p}$ and $\varepsilon_{\rm p}$ define the size and the smoothness of the edge, respectively ($\varepsilon_{\rm p} \to 0$ corresponds to a uniform disk). The appropriate values for $r_{\rm p}$ and $\varepsilon_{\rm p}$ were found to be 12 mas and 2.4 mas, respectively. We adopted the maximum entropy regularization as in Paper II.

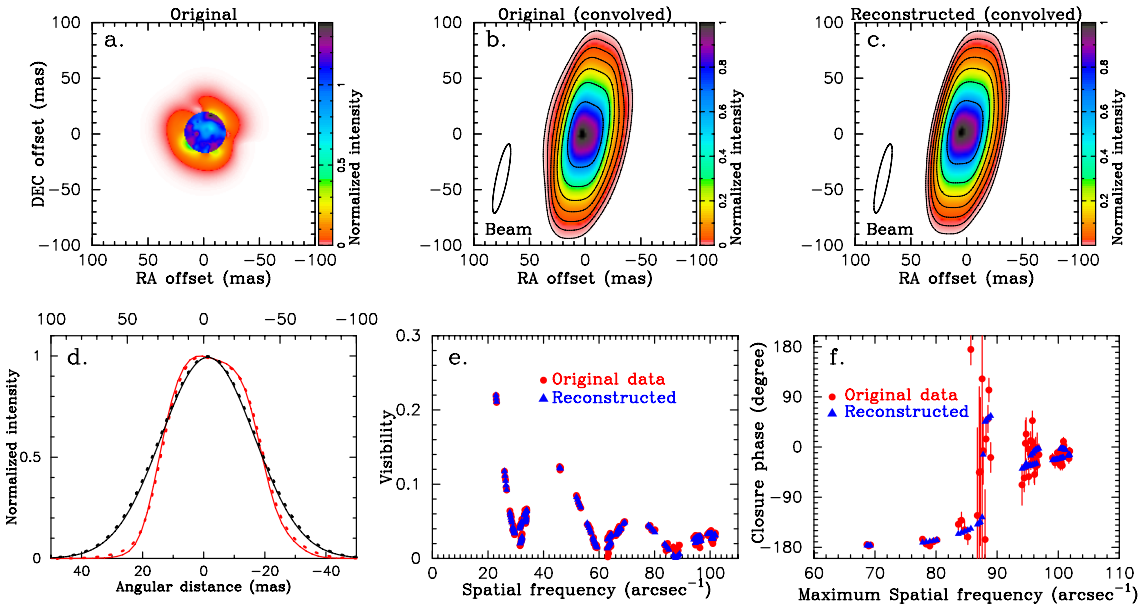

Fig. B.2. Image reconstruction from the simulated data for a uniform disk with surface inhomogeneities and an asymmetric extended component, shown in the same manner as Fig. B.1.

Appendix C: Fit to the interferometric data

Figures C.1 and C.2 show the fit to the measured interferometric observables for the image reconstruction in the CO line shown in Figs. 5 and 7, respectively.

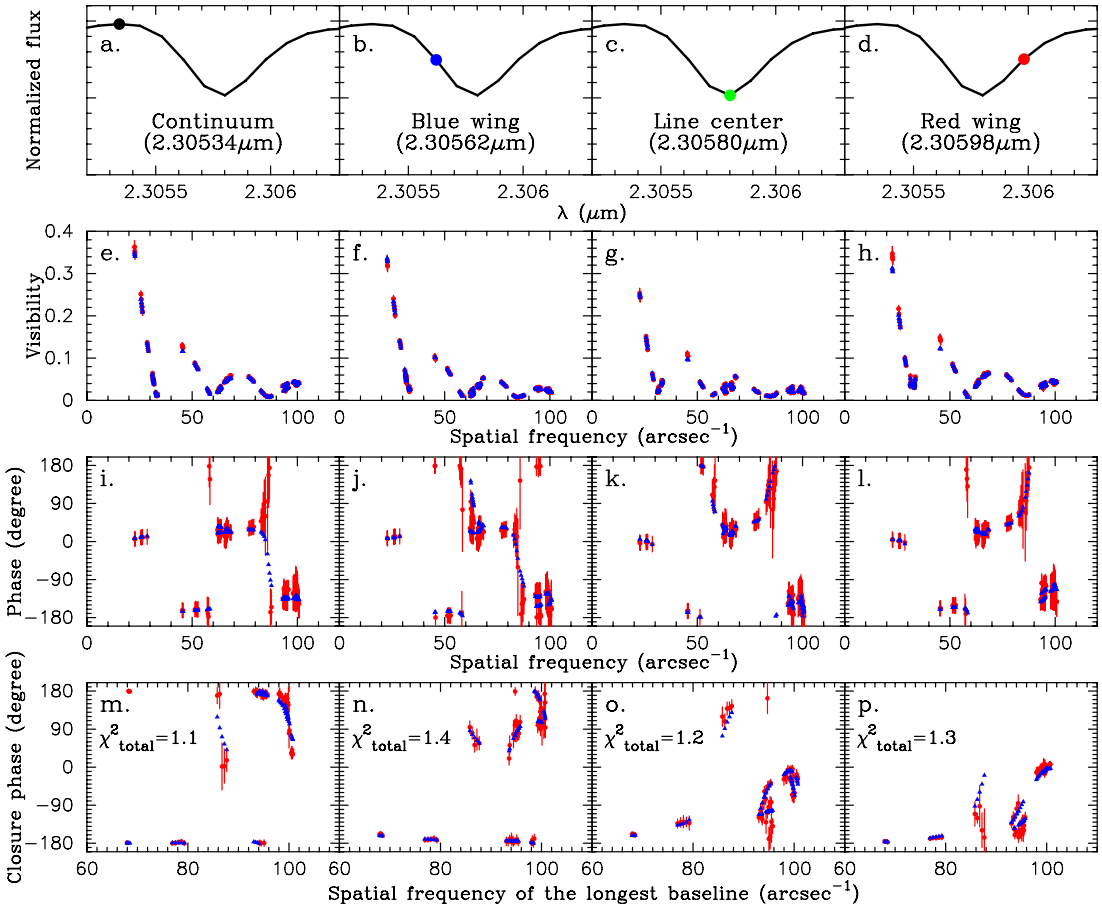

Fig. C.1. Comparison between the interferometric observables measured in 2009 and those from the reconstructed images within the CO line profile shown in Fig. 5. The *first, second, third, and fourth columns* show the comparison for the continuum, blue wing, line center, and red wing, respectively. The filled circles in the *top row* (**a**)–(**d**)) show the positions within the CO line profile. In the *remaining panels*, the observed data and those from the image reconstruction are plotted by the dots and triangles, respectively. The reduced χ^2 values including the visibilities, phases, and closure phases, are given in the panels in the *bottom row*.

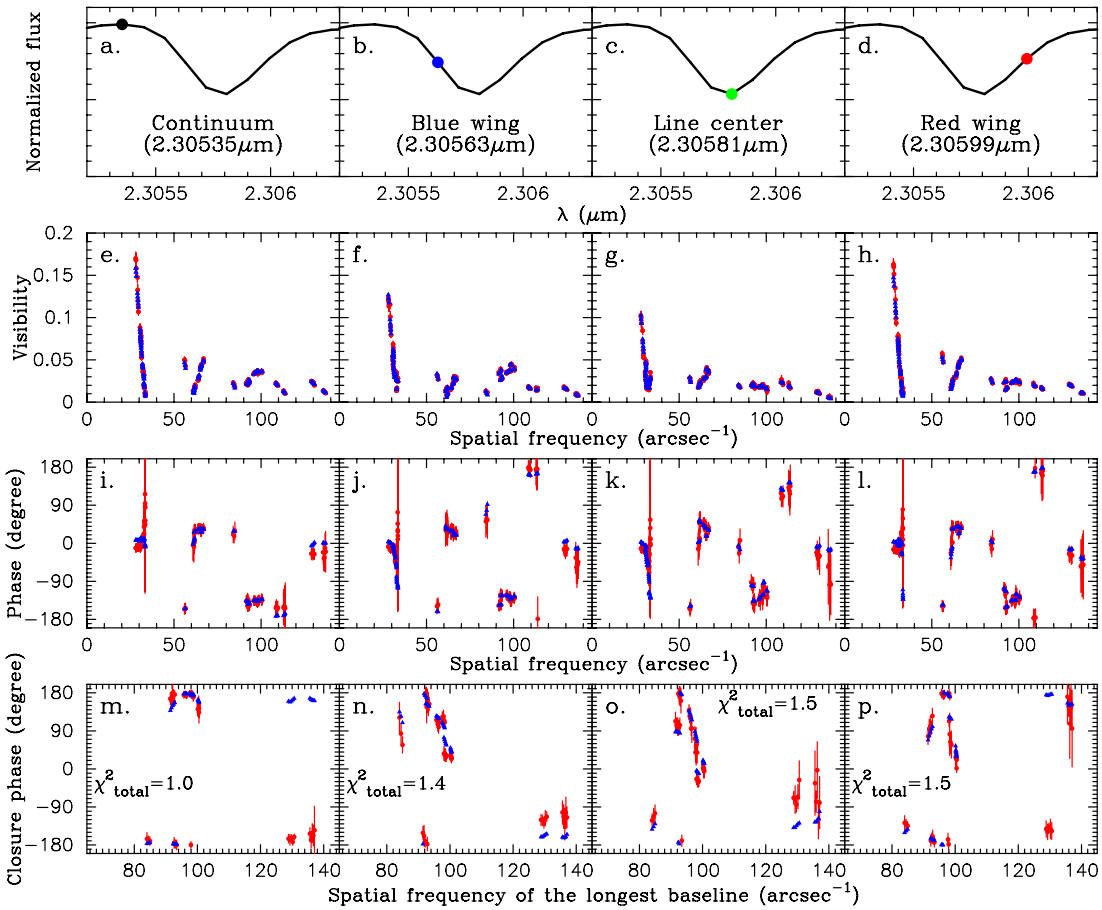

Fig. C.2. Comparison between the interferometric observables measured in 2010 and those from the reconstructed images within the CO line profile shown in Fig. 7. The panels are shown in the same manner as in Fig. C.1.